scientific reports

Check for updates

OPEN

A new occurrence of hydrous andradite within pyroclastic rocks of the Sierra De Bahoruco, Dominican Republic

Jacek Wachowiak[1], Magdalena Dumańska-Słowik[2]✉, Wiesław Heflik[2], Adam Włodek[2], Lucyna Natkaniec-Nowak[2], Miguel Peña[3], Adam Gaweł[2], Rolando Muñoz[4] & Piotr Jeleń[5]

The titanium-bearing (up to 3.31 wt% TiO_2) hydrous andradite $[Ca_{2.98}Na_{(0.02)}K_{(0.01)}Fe^{2+}_{(0.01)}]_{\Sigma=3.02}[Fe^{3+}_{1.25}Al_{0.45}Ti_{0.15}Fe^{2+}_{0.07}Mg_{0.04}V^{3+}_{0.01}Mn^{2+}_{0.01}]_{\Sigma=2.98}Si_{2.43}O_{9.72}(OH)_{2.28}$ was identified within intensely altered and weathered pyroclastic rocks in the Sierra de Bahoruco region in the Dominican Republic. It forms small isolated euhedral crystals, infillings of fissures and fractures, and large polycrystalline aggregates, in close paragenesis with clinochlore and calcite. Other phases present in the secondary assemblage, formed as a result of hydrothermal and/or supergenic processes, include prehnite, pumpellyite, and natrolite. The formation of this secondary assemblage was a result of metasomatism under low temperature zeolite facies conditions. The formation of hydrous garnet required high-pH aqueous fluids enriched in Ca and Fe. The Ca needed for garnet crystallization might have derived from primary calcic plagioclases, diopside, and Eocene-Miocene limestones overlying the Cretaceous magmatic complex. Geothermometry on coexisting chlorite revealed that the metasomatic hydrous andradite was formed under low-temperature conditions (~160 °C). Iron and Ti oxidation states in the andradite indicate that its formation occurred under relatively oxidizing conditions. The hydrous titanian garnet represents one of the latest phases of the pervasive calcium metasomatic event in the Sierra de Bahoruco area.

Keywords Hydrous andradite, Low-temperature, Metasomatism, Las Filipinas Larimar Mine, Dominican Republic

Garnets are nesosilicates that belong to one of five groups within the garnet supergroup[1]. They are characterized by a cubic structure and a general formula of $X_3Y_2(SiO_4)_3$, where X = Ca, Mg, Mn^{2+}, Fe^{2+}, etc., and Y = Al, Mg, V^{3+}, Cr^{3+}, Fe^{3+}, Sc[1]. There are fourteen species distinguished within the garnet group with a total charge at the tetrahedral site of 12 [1], with pyrope, grossular, spessartine, almandine, uvarovite, and andradite species as the most well-known anhydrous members. In nature, there are also garnets containing substantial amounts of the hydroxyl ion (OH^-) replacing partially or completely $[SiO_4]^{4-}$ tetrahedra[2–4]. Many of them have compositions intermediate between grossular (x = 0) and katoite (x = 3), i.e., $Ca_3Al_2(Si_{3-x}\square_x)O_{12-4x}(OH)_{4x}$ where $0 < x < 3$ and $\square$ is vacancy[5]. Similarly, the Fe-containing hydrous garnet is designated as hydrous andradite $Ca_3Fe_2(Si_{3-x}\square_x)O_{12-4x}(OH)_{4x}$[3]. The replacement of $[SiO_4]^{4-}$ tetrahedra by $(O_4H_4)^{4-}$ can result in a range of intermediate compositions, while, the extent of the solid solution depends strongly on the temperature conditions[3,6].

The minerals of the garnet group are particularly hosted by metamorphic rocks, though they are also found in igneous rocks and as detrital grains in sediments[7,8]. In contrast to the anhydrous species, the data on the occurrence of hydrous garnets in nature are relatively limited. The majority of reports on hydrous garnets originate from metamorphic rocks such as serpentinites[9–12], rodingites[13–16], skarns[17], and alkaline igneous rocks[18]. No data are provided for the occurrence of hydrous garnets in pyroclastic rocks. In the Caribbean,

[1]The Research and Development Centre for Mining of Chemical Raw Materials "CHEMKOP", 7 Wybicki Str., Kraków 31-261, Poland. [2]Faculty of Geology, Geophysics and Environmental Protection, AGH University of Krakow, 30 Mickiewicz Av, Kraków 30-059, Poland. [3]UTECO-Universidad Tecnológica del Cibao Oriental, Ciudad Universitaria Uteco, Cotui, Sanchez Ramirez, Dominican Republic. [4]Dirección General de Minería, Geologo-A, Edificio Juan Pablo Duarte 10mo Piso Ave. México Esq. Leopoldo Navarro, Santo Domingo 10201, Dominican Republic. [5]Faculty of Materials Science and Ceramics, AGH University of Krakow, 30 Mickiewicz Av, Kraków 30-059, Poland. ✉email: dumanska@agh.edu.pl

uvarovite species, presumably containing some water, were only reported from ophiolitic chromitites of the Dominican Republic and Cuba[19,20]. In addition to terrestrial phases, the hydrous andradite has been reported in Mighei-like carbonaceous chondrites[21], which provides evidence for the existence of asteroidal hydrous garnets. This paper first documents the occurrence of Ti-rich hydrous andradite hosted by pyroclastic rocks from the Las Filipinas larimar (a gem quality blue pectolite intergrown with white and green pectolite, natrolite, prehnite, chlorite, and calcite)[22] mine in the Barahona Province in the southwest of the Dominican Republic. The characterization of hydrous garnet was conducted using electron microprobe analyses (EMPA) supported by Raman micro-spectroscopy, scanning electron microscopy with energy dispersive spectrometry (SEM-EDS), and X-ray powdered diffraction (XRPD) to gain insights into the formation environment, including the temperature, origin, and composition and source of mineralizing fluids. Consequently, chlorite (which chemistry is sensitive to, *inter alia*, the temperature of formation, redox state, and composition of host rocks[23]) occurring in close paragenesis with hydrous andradite has been effectively applied as a geothermometer[24,25] to estimate the physicochemical conditions prevailing during the formation of both coexisting phases. Hence, we propose a genetic model for the formation of a Ti-enriched hydrous garnet at the expense of the primary mineral assemblage of pyroclastic rocks under the influence of hydrothermal fluids and pervasive metasomatism.

Geological setting

The Las Filipinas larimar mine is found in the Sierra de Bahoruco massif, near Los Chupaderos and about 15 km of Barahona (SW Dominican Republic; Fig. 1A). The Sierra de Bahoruco area is dominated by fine-crystalline, pelagic limestones of the Eocene-lower Miocene Neiba Formation. These are underlain by volcanic rocks of the Dumisseau Formation associated with suboceanic magmatism of Cretaceous age (Fig. 1B, C)[26–29]. The Dumisseau Formation represents a fragment of the Caribbean Large Igneous Province (CLIP) uplifted and accreted onto the northern margin of the Caribbean Plate[30]. It comprises an ~ 1.5 km-thick sequence of submarine basalt flows (85 – 70 Ma) and pyroclastic deposits intruded by younger dolerite dykes and sills at 53 Ma[31,32]. Three types of volcanic facies in this area were distinguished by Escuder-Viruete et al.[32]: (i) coherent, mafic flows and autoclastic breccias, (ii) mafic breccias and tuffs formed by subaqueous eruptions, and (iii) re-sedimented syneruptive polygenetic breccias with fine-grained volcanoclastic rocks. The uppermost part of the volcanic series is composed of several subaerial eruption cycles, which combine two main distinctive eruptive zones, each from several dozens of centimetres to several meters in size, and composed of (1) basaltic rocks and (2) basaltic pyroclastic material[33]. All these facies underwent pervasive, post-magmatic, hydrothermal alteration, which led to the formation of new products, e.g., the unique blue-green-white pectolite mineralization (known as larimar), prehnite, pumpellyite, albite, calcite, chlorite, epidote, and Fe oxides[32,34]. Basaltic rocks are bluish-grey, green to brown with porphyritic and amygdaloidal texture[32]. Pectolite, calcite, natrolite, and prehnite represent the main amygdaloidal facies[22]. Pyroclastic rocks are commonly grey or dark green displaying various grades of alteration and weathering. They are composed of consolidated rock fragments and irregularly distributed fragments of tree trunks and branches showing various degrees of charring.

Results

Petrography

The pyroclastic rocks are mainly composed of lithoclasts, crystal clasts, and minor amounts of vitroclasts. The lithic clasts exhibit a porphyritic texture and comprise clinopyroxene and relicts of calcic plagioclase phenocrysts. Clinopyroxenes of diopside-hedenbergite series form non-pleochroic, prismatic and lamellar crystals that have been partially or completely altered to colourless or slightly pleochroic (i.e., greenish) chlorite (Fig. 2A–D). Locally, some relics of orthopyroxene of the enstatite-ferrosilite series are found. The calcic plagioclase is pervasively altered to chlorite and smectite (Fig. 2E, F). Accessory components found in the lithoclasts include magnetite, ilmenite, and rutile. The groundmass is composed of a partially devitrified, mafic, glassy paste and opaque minerals. The crystal clasts are represented by the same minerals found in the lithoclasts. The vitroclasts show a slightly yellow-brown colour, diagnostic of palagonitised glass. The pyroclastic rocks contain also secondary minerals such as calcite and prehnite forming veins that crosscut the previously described rock components, as well as pectolite, natrolite, and pumpellyite forming infillings of fractures and cavities. Additionally, they contain garnets, which are mostly isotropic in thin sections (Fig. 2D), but species showing anomalous anisotropy has been also observed as numerous small crystals hosted by chlorite and calcite (Fig. 3A–D).

The garnets found in pyroclastic rocks of the Sierra de Bahoruco area occur in three textural types. The first type is formed as isolated, euhedral crystals with diameters of ~ 5 µm typically found within the chloritized and carbonated groundmass of the lithoclasts (Fig. 4A). Some of these crystals are characterized by sector zoning with visible chemical variation between core zones and rims (Fig. 4B). Under the polarizing microscope they have isotropic inner domains and anisotropic external regions. The second type is an accumulation of non-zoned, homogenous crystals in the forms of veins and nests with thicknesses of several to several hundred micrometres (Fig. 4C). It usually coexists with chlorite. The third textural type occurs as polycrystalline aggregates found within tabular forms of sizes up to 700 µm (Fig. 4D) and is found within lithoclasts and crystal clasts. Garnets of the third textural type also do not show internal zoning and are locally intergrown with chlorite and calcite (Fig. 4D).

Mineral chemistry

Garnet

In general, garnets from the three textural types described above can be characterized using a unified crystallochemical formula $[Ca_{2.98}Na_{(0.02)}K_{(0.01)}Fe^{2+}{}_{(0.01)}]_{\Sigma=3.02}[Fe^{3+}{}_{1.25}Al_{0.45}Ti_{0.15}Fe^{2+}{}_{0.07}Mg_{0.04}V^{3+}{}_{0.01}Mn^{2+}{}_{0.01}]_{\Sigma=2.98}Si_{2.43}O_{9.72}(OH)_{2.28}$. The H_2O content, given on the stoichiometry of minerals

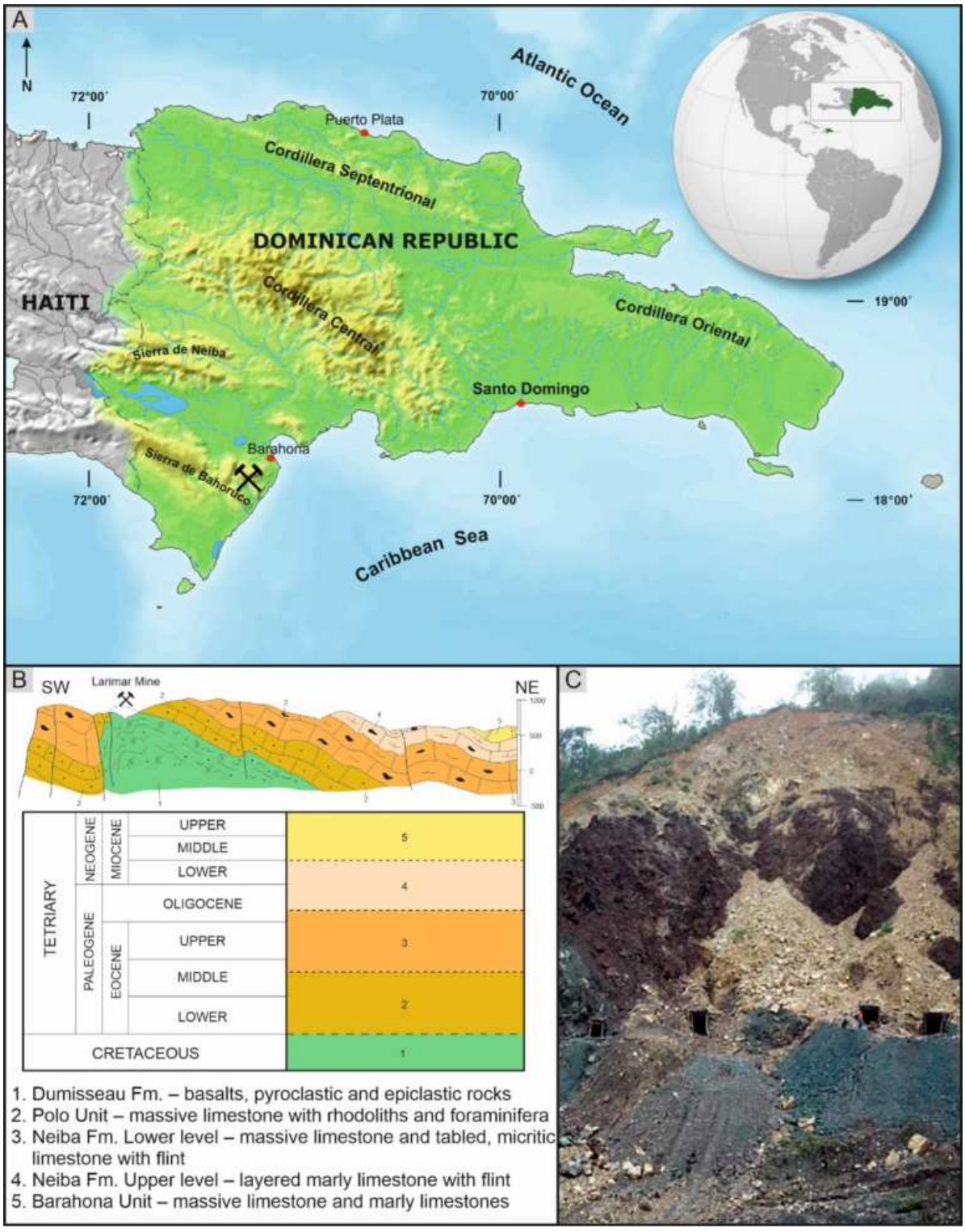

Fig. 1. (**A**) The localization of the Las Filipinas larimar mine in Sierra de Bahoruco, Barahona Province, southern Dominican Republic, modified after Wachowiak et al.[34]; (**B**). The simplified geological cross-section of the basaltic massif of the Dumisseau Formation, Sierra de Bahoruco, Barahona Province, Dominican Republic, modified after Wachowiak et al.[34] ; (**C**). Field exposure from the Las Filipinas larimar mine showing the contact between volcanic rocks (i.e. basalts and pyroclastic deposits) and overlying sedimentary deposits (limestones), photo made by Wachowiak J; Fig. 1 created with CorelDraw 2024.

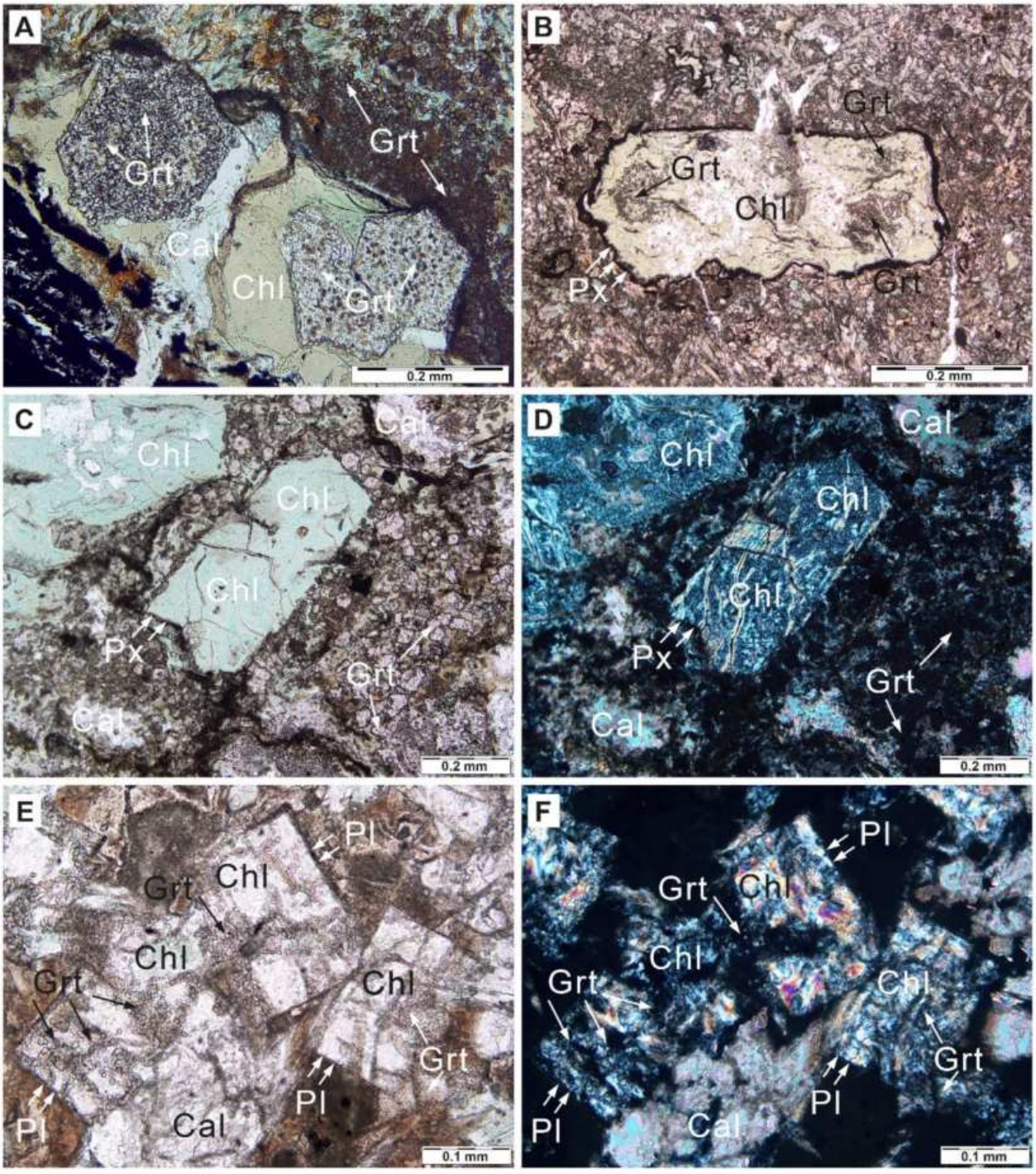

Fig. 2. Photomicrographies of pyroclastic rocks from the Las Filipinas larimar mine in Barahona Province in southwestern Dominican Republic: (**A**) Primary minerals completely replaced by garnets (Grt) at the contact with calcite (Cal) and chlorite (Chl); (**B**) Relics of pyroxene (Px) replaced by chlorite (Chl) hosting abundant small grains of garnet (Grt); (**C**,**D**) Relics of pyroxene (Px) replaced by chlorite (Chl). Note the presence of calcite (Cal) and numerous small isotropic garnets (Grt) seeun under crossed polarizers (**D**); (**E**,**F**) Relics of alkali feldspars (Pl) showing characteristic lath shapes, filled with chlorite (Chl) and garnet (Grt), Note the palagonised glass in the background of the rock.

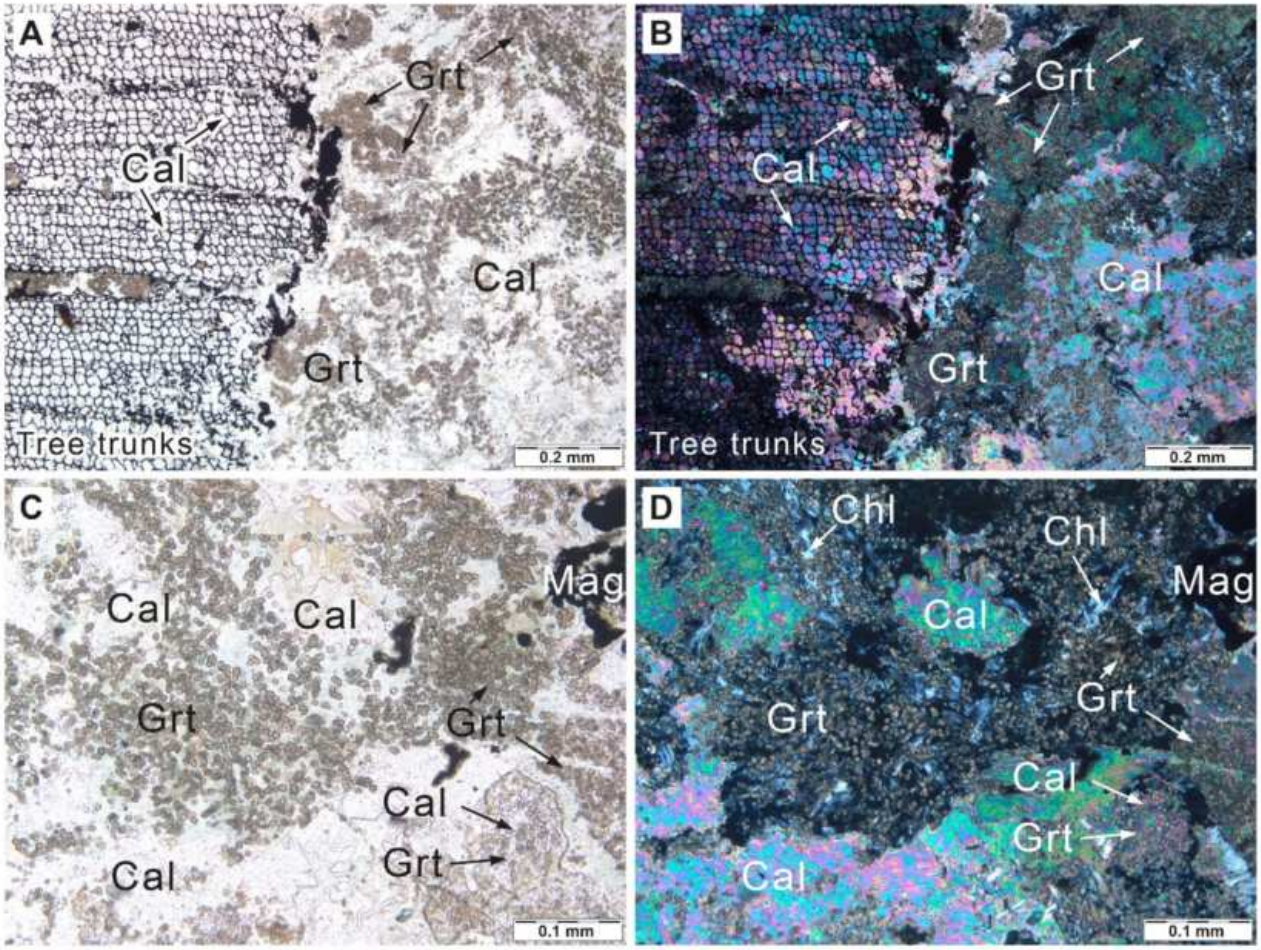

Fig. 3. Photomicrographies of pyroclastic rocks from the Las Filipinas larimar mine in Barahona Province in southwestern Dominican Republic: (**A**,**B**) the contact of the charred tree trunks with strongly transformed pyroclastic rock. Note the wood tissue replaced with calcite (Cal), while pyroclastic rocks composed of calcite (Cal) with garnets (Grt) showing anomalous anisotropic properties, probably inherited from host calcite; (**C**,**D**) Strongly altered pyroclastic rock composed of calcite (Cal), garnets (Grt) and magnetite (Mag).

of the garnet supergroup, calculated according to the recommendations of Grew et al. (2013), fluctuates in the range of 2.43–6.51 wt%, which corresponds to the range of 0.35–0.90 $(OH)_4$ atoms per formula unit (apfu). The contents of individual components are found in the ranges of 0.00-0.40 wt% Na_2O, 0.00-1.51 wt% MgO, 2.30–9.30 wt% Al_2O_3, 25.70-31.47 wt% SiO_2, 0.00-2.90 wt% P_2O_5, 31.90-35.82 wt% CaO, 0.08–5.92 wt% TiO_2, 0.00-1.26 wt% V_2O_3, 0.00-0.37 wt% Cr_2O_3, 0.00-0.27 wt% MnO, 0.00-4.28 wt% FeO and 14.27–26.71 wt% Fe_2O_3 (Table 1). The garnets found in pyroclastic rocks of the Sierra de Bahoruco region are mainly represented by the species of the andradite – hydrous andradite series $Ca_3Fe^{3+}{}_2Si_3O_{12}$ – $Ca_3Fe^{3+}{}_2Si_2O_8(OH)_4$ (Figs. 5 and 6), which chemically correspond to the Fe^{3+} analogue of holtstamite $Ca_3Al_2Si_2O_8(OH)_4$, tetragonal hydroxyl-bearing garnet[1].

The core zones of small euhedral garnet crystals (textural type 1, Fig. 4B) are chemically distinct and can be classified as Fe^{2+}-bearing hydrous andradite with a generalized crystal-chemical formula $[Ca_{2.22}Fe^{2+}_{(0.74)}Na_{(0.02)}Mn_{(0.01)}Mg_{(0.01)}]_{\Sigma=3.00}[Fe^{3+}{}_{1.50}Al_{0.35}Ti_{0.08}Mg_{0.04}Fe^{2+}{}_{0.02}V^{3+}{}_{0.01}]_{\Sigma=3.00}Si_{1.93}O_{7.72}(OH)_{4.28}$. Compared to andradite – hydrous andradite series, this species is characterized mainly by elevated contents of iron oxides, i.e. 9.71–18.66 wt% FeO and 23.07–28.95 wt% Fe_2O_3 (Table 1), and much lower contents of silica (20.02–26.55 wt% SiO_2) and calcium (23.05–27.53 wt% CaO). Among the chemical substitutions in the composition of garnets, the most visible are the negative correlations of Al-Fe^{3+} (also visible in the Al-Fe_{total}) and Fe^{2+}-Ca and Mg-Ca. They correspond well to substitutions resulting from garnet crystallochemistry, including isovalent substitutions of Al-Fe^{3+} (*Y* position) and Fe^{2+}-Ca and Mg-Ca (*X* position), while the substitutions showing positive correlations include Fe^{2+}-Ti and Al-V^{3+} (Fig. 7). The Fe^{2+}-Ti correlation results from the charge compensation of the heterovalent substitution of $Fe^{2+}+Ti^{4+} \leftrightarrow 2Fe^{3+}$. The positive correlation between Al and V^{3+} is probably influenced by the initial chemical composition of the hydrothermal fluid. A similar positive correlation was previously documented for grossular from Čierna Lehota[35] and Al-rich andradite from the Laoshankou deposit[36].

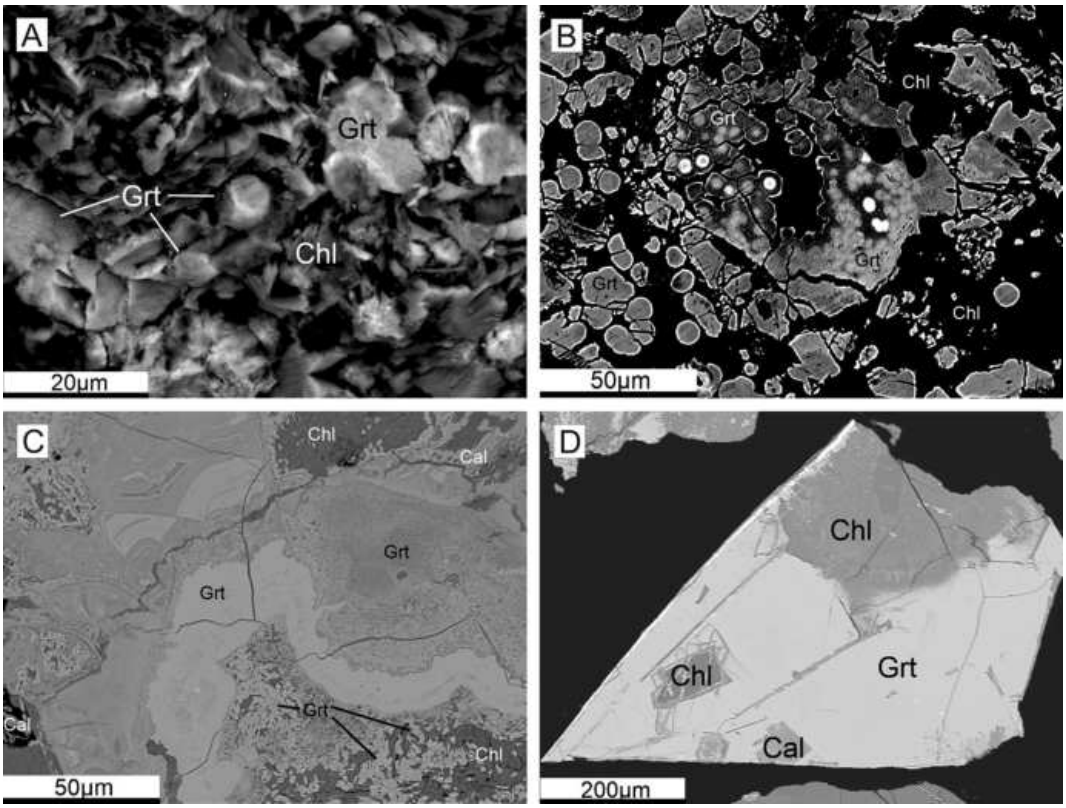

Fig. 4. BSE images of various textural types of andradite: A – type 1 - small euhedral grains of garnet (Grt) within chlorite (Chl), B- type 1- some grains exhibit characteristic chemical zoning; C- type 2- the infillings of some zones with garnet (Grt) in close paragenesis with chlorite (Chl); D- type 3 compact masses of garnet (Grt) replacing primary phases. Garnet hosts inclusions of chlorite (Chl) and calcite (Cal).

Clinopyroxene and chlorite

The relicts of clinopyroxene crystals are rich in CaO (22.30-24.01 wt%), MgO (12.81–15.07 wt%) and SiO_2 (50.92–53.14 wt%), while other components such as FeO (1.66–6.96 wt%), TiO_2 (1.30–5.04 wt%), Na_2O (0.68–1.85 wt%), Al_2O_3 (0.17–1.51 wt%), Fe_2O_3 (0.00-0.60 wt%), MnO (0.12–0.27 wt%), Cr_2O_3 (0.00-0.27 wt%) appear in minor amounts (Table 2). The average formula of the species was calculated as $(Ca_{0.92}Na_{0.09})$ $(Ti_{0.08}Fe^{3+}_{0.01}Mg_{0.79}Fe^{2+}_{0.13}Mn_{0.01})(Si_{1.95}Al_{0.03})O_6$ and corresponds to diopside based on the quadrilateral of ternary $Ca_2Si_2O_6$ (wollastonite)-$Mg_2Si_2O_6$ (enstatite)-$Fe^{2+}{}_2Si_2O_6$ (ferrosilite) classification diagram[37] (Fig. 8).

The chlorites are characterized by a high content of Si (3.23–3.37 apfu) with subordinate tetrahedral Al (0.63–0.77 apfu). In the octahedral sites, Mg (3.72–3.92 apfu) distinctly predominates over Fe^{2+} (1.09–1.70 apfu) with other components such as Al^{VI} (0.35–0.90 apfu), Fe^{3+} (0.00-0.33 apfu), Ti (0.00-0.06 apfu), Cr (0.00-0.01 apfu) and Mn (0.01–0.04 apfu) found in subordinate amounts. The sum of octahedral cations falls between 5.76 and 6.00 apfu with the octahedral vacancy in the range of 0.00-0.24 apfu (Table 3). The content of alkalis in interlayer sites is variable and ranges from 0.03 to 0.15 apfu. Following the classification scheme proposed by Zane and Weiss[38], based on Mg + Fe > Al + vacancy as well as the dominant octahedral cation, the chlorite species belongs to Type I (trioctahedral) Mg-chlorite. Its composition is close to the clinochlore end-member of the clinochlore-chamosite series (Fig. 9).

Since the composition of chlorite is sensitive to physicochemical conditions that prevailed at the time of its formation, including pressure, temperature, pH, and the activity of various ions dissolved in the fluid[39,40], the clinochlore coexisting with hydrous garnet was used to constrain the temperatures of crystallization. The temperature of chlorite crystallization has been assessed using two empirical geothermometers based on tetrahedral Al[24,25]. As a result, it was found that the formation temperature of chlorite varies in ranges of 148–177 °C and 142–187 °C (Table 3)[24,25]. Additionally, the local presence of high Na + Ca + K in chlorites is typical of low-temperature chlorites found in basaltic rocks[41], or may be related to the coexistence of other low-temperature phases typical of altered basaltic rocks such as smectite and illite phases[42]. Similarly, the high Si contents in clinochlore are consonant with low-temperature conditions of its crystallization[40] but can also respond to mixed analyses.

Raman micro-spectroscopy characteristics

The Raman spectra collected for hydrous garnet found within carbonated groundmass (Fig. 10) are dominated by Raman bands of andradite[43,44] with additional lines due to coexisting calcite[45]. The principal Raman bands produced by garnet are single, broad lines with maxima at 353, 509, and 3576 cm^{-1} (and 353, 508 and 3554 cm^{-1}

Textural type	GC		Fe-GC		GR				CLG		CMG		
An. no.	ZD2_5#01	178_2#04	178_2#02	178_2#03	1_12_#04	1_14_#08	178_2#03	178_m2#28	1_8#3	1_8#6	1_1#05	1_4#07	ZD1_2#02
P_2O_5	bdl	bdl	bdl	bdl	bdl	0.03	bdl	bdl	0.09	0.12	bdl	0.05	bdl
SiO_2	28.72	31.19	26.55	24.86	29.61	25.70	29.17	26.99	29.81	31.29	30.54	26.98	31.47
TiO_2	1.87	3.20	2.10	1.83	2.72	3.71	1.46	0.08	0.95	0.84	3.37	2.53	0.78
Al_2O_3	9.30	3.04	4.00	4.42	5.68	4.92	6.52	6.43	2.87	2.51	4.33	6.50	2.34
V_2O_3	0.19	0.24	0.14	0.19	0.65	0.13	1.26	0.90	0.06	0.11	0.42	0.35	0.41
Cr_2O_3	bdl	bdl	bdl	bdl	0.37	0.12	0.05	bdl	bdl	bdl	bdl	bdl	bdl
Mn_2O_3	bdl	bdl	bdl	bdl	bdl	bdl	bdl	bdl	bdl	bdl	bdl	bdl	bdl
Fe_2O_3**	15.95	20.95	23.08	23.45	18.02	17.73	19.14	21.14	25.65	26.44	18.86	18.63	26.71
FeO**	1.00	2.63	9.71	11.07	0.93	2.62	0.48	bdl	0.35	0.40	1.99	0.61	bdl
MgO	0.16	0.17	0.67	0.40	0.55	0.06	0.26	0.09	0.14	0.24	0.23	0.70	0.06
CaO	35.82	33.40	27.53	27.14	34.04	33.90	33.75	34.52	33.93	33.77	34.02	33.80	33.76
MnO	bdl	bdl	0.14	0.11	0.12	bdl	0.09	bdl	0.09	bdl	0.11	bdl	0.06
Na_2O	0.11	0.08	0.12	0.13	0.12	0.19	0.14	0.13	bdl	bdl	0.09	0.15	0.09
H_2O*	5.80	2.95	6.58	7.90	4.24	6.47	4.45	5.88	3.76	2.89	3.53	5.98	2.73
Sum	98.93	97.83	100.61	101.48	97.06	95.58	96.76	96.17	97.68	98.61	97.48	96.26	98.39
apfu													
P	0.000	0.000	0.000	0.000	0.000	0.002	0.000	0.000	0.007	0.008	0.000	0.003	0.000
Si	2.240	2.589	2.118	1.955	2.421	2.106	2.391	2.202	2.470	2.590	2.515	2.184	2.619
$(OH)_4$	0.760	0.411	0.882	1.045	0.579	0.891	0.609	0.798	0.523	0.402	0.485	0.813	0.381
Sum*(T)*	3.000	3.000	3.000	3.000	3.000	3.000	3.000	3.000	3.000	3.000	3.000	3.000	3.000
Ti	0.110	0.200	0.126	0.108	0.167	0.229	0.090	0.005	0.059	0.052	0.209	0.154	0.049
Al	0.855	0.297	0.376	0.409	0.548	0.475	0.630	0.618	0.280	0.244	0.420	0.620	0.229
V	0.006	0.008	0.004	0.006	0.021	0.004	0.041	0.029	0.002	0.004	0.014	0.011	0.014
Cr	0.000	0.000	0.000	0.000	0.016	0.005	0.002	0.000	0.000	0.000	0.000	0.000	0.000
Fe^{3+}	0.936	1.308	1.386	1.388	1.108	1.094	1.180	1.298	1.599	1.647	1.169	1.135	1.672
Fe^{2+}	0.065	0.183	0.648	0.728	0.063	0.179	0.033	0.000	0.024	0.028	0.137	0.041	0.000
Mn	0.000	0.000	0.010	0.007	0.008	0.000	0.006	0.000	0.006	0.000	0.008	0.000	0.004
Mg	0.019	0.021	0.080	0.046	0.067	0.007	0.032	0.011	0.017	0.030	0.028	0.085	0.008
Ca	2.993	2.970	2.353	2.287	2.982	2.977	2.963	3.018	3.012	2.995	3.001	2.931	3.010
Na	0.016	0.013	0.018	0.020	0.019	0.030	0.023	0.021	0.000	0.000	0.015	0.023	0.014
Sum*(X+Z)*	5.000	5.000	5.000	5.000	5.000	5.000	5.000	5.000	5.000	5.000	5.000	5.000	5.000

Table 1. Representative EMPA data of hydrous garnet.

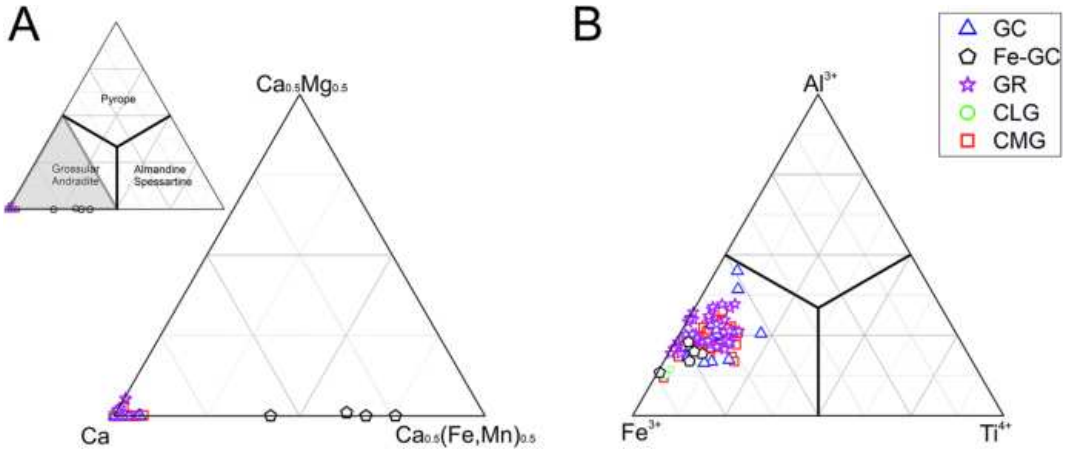

Fig. 5. The composition of hydrous garnet plotted into ternary classification diagrams of garnet: A - Ca-$Ca_{0.5}Mg_{0.5}$- $Ca_{0.5}(Fe, Mn)_{0.5}$; B – Fe^{3+} Al^{3+} - Ti^{4+}. Note: Textural types of garnet: GC – individual garnet core (1); Fe-GC – iron-rich individual garnet core (1); GR – individual garnet rim (1); CLG – garnet of continues layers (2); CMG – compact-masses garnet (3).

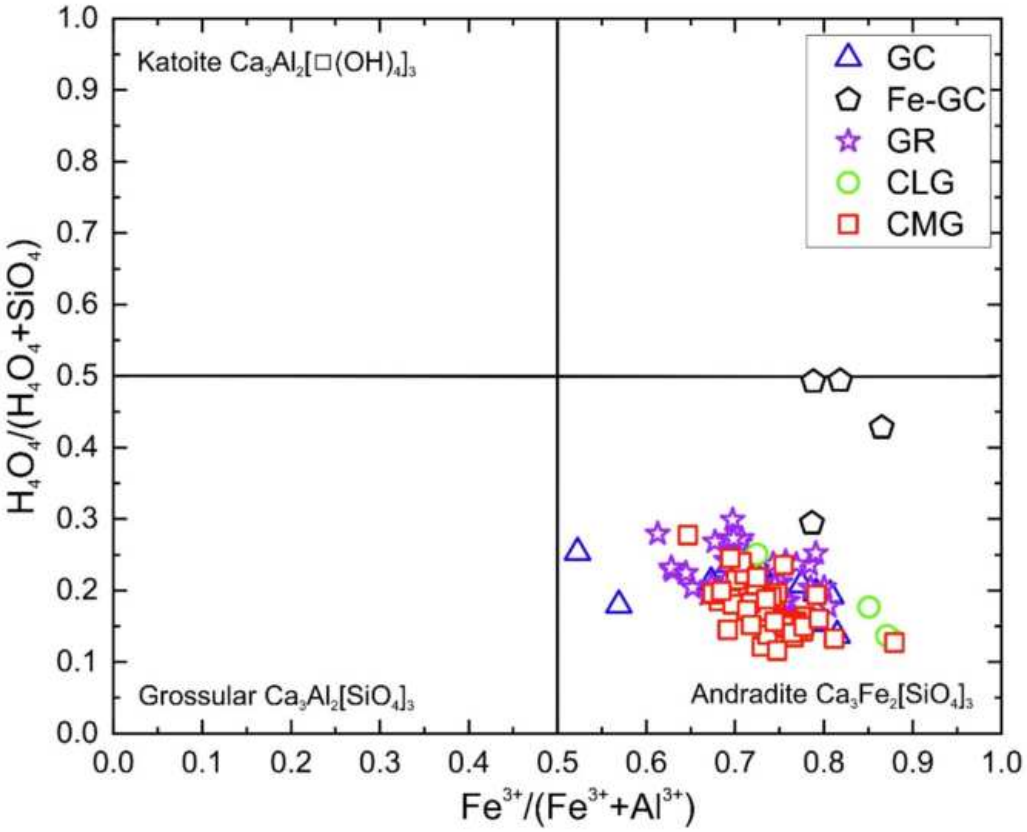

Fig. 6. The composition of hydrous garnet plotted into $Fe^{3+}/(Fe^{3+}+Al^{3+})$ vs. $H_4O_4/(H_4O_4+SiO_4)$ diagram. Note: Textural types of garnet: GC – individual garnet core (1); Fe-GC – iron-rich individual garnet core (1); GR – individual garnet rim (1); CLG – garnet of continues layers (2); CMG – compact-masses garnet (3).

for the 532 nm laser, respectively) and a wide triplet band with maxima at 819, 845 and 864 cm^{-1} (818, 851 and 870 cm^{-1} for the 532 nm laser, respectively) (Table 4). The presence of these three bands in the region of 800–1050 cm^{-1} is a diagnostic feature for andradite and enables its distinction from grossular[44]. The broad band in the range of 3500–3600 cm^{-1} is due to OH vibrations (Table 4), thereby confirming the presence of structural water in garnet[9,13]. Weaker bands are observed at the regions with local maxima of 157, 240 and 995 cm^{-1} (160, 245 and 999 cm^{-1} for the 532 nm laser, respectively). The bands originating from the carbonates are found at 285, 714 and 1087 cm^{-1} (737 and 1112 cm^{-1} for the 532 nm laser; Fig. 10). The weak bands located in the region of 1200–1900 cm^{-1} are likely to be derived from the epoxy resin (araldite) used to bind the sample[46].

X-ray diffraction

The powdered X-ray diffraction pattern showed a dominance of garnet (morimotoite-schörlomite) with an admixture of calcite and clinochlore (Fig. 11). Additionally, it yielded traces of pectolite, prehnite, magnetite, manganite, enstatite, trioctahedral illite, and trioctahedral smectite. The phases were identified based on the following data: morimotoite ICDD database entry no. 47-1877, schörlomite ICDD database entry no. 33–285, calcite ICDD database entry no. 05-0586, clinochlore ICDD entry no. 16–0362, magnetite ICDD entry no. 19–0629, manganite ICDD entry no. 41-1379, a solid solution of enstatite (ICDD entry no. 19–768).- ferrosilite (ICDD entry no 29–721), pectolite (74-1109), and prehnite (29–0290). The identification of trioctahedral clay minerals, i.e., chlorite, smectite and illite in the sample was made based on XRPD patterns of samples under air-dry, calcinated at 560 °C, and ethylene-glycol-saturated conditions. The presence of other mixed-layer clay minerals cannot be excluded.

The calculation of unit-cell parameters of garnet was carried out based on nine reflections of garnet that do not overlap with the reflections of calcite and chlorite (Table 5). The unit-cell parameter, refined for the cubic space group *Ia*-3*d*, is a = 12.172(5) Å. The results obtained are consistent with the data reported for morimotoite (ICDD database entry no. 47-1877 – i.e. 12.162(3) Å)[47] and hydrous grossular (ICDD database entry no. 75–169 – i.e. 12.174 Å[48], , and different than that for OH-rich andradite from various parts of the world, i.e., the Kalahari

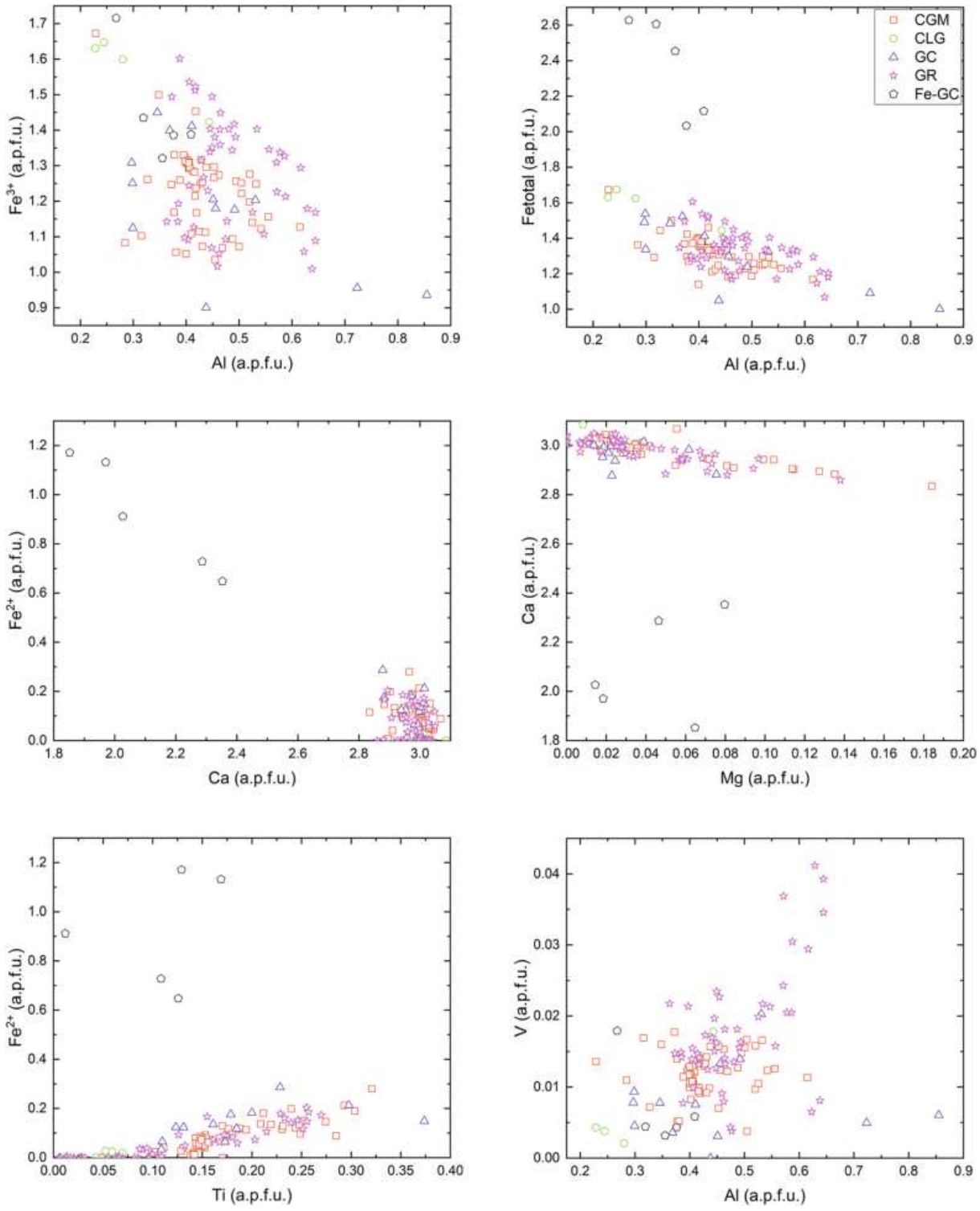

Fig. 7. Substitution diagrams garnet crystals from the Las Filipinas larimar mine in Barahona Province in southwestern Dominican Republic. Note: Textural types of garnet: GC – individual garnet core (1); Fe-GC – iron-rich individual garnet core (1); GR – individual garnet rim (1); CLG – garnet of continues layers (2); CMG – compact-masses garnet (3).

Component (wt%)	H1_1	H1_2	H1_3	H1_4	H1_5	H1_6	H1_7	H1_8	H1_9	H1_10
SiO_2	50.92	51.89	52.90	52.68	52.49	52.48	51.38	52.15	53.14	51.10
TiO_2	4.29	3.53	1.33	1.45	1.56	1.69	4.49	3.30	1.30	5.04
Al_2O_3	1.51	1.10	0.18	0.17	0.17	0.20	1.28	0.79	0.26	1.32
Cr_2O_3	0.10	0.22	0.00	0.07	0.00	0.05	0.27	0.14	0.06	0.08
Fe_2O_3 (*calc.*)	0.10	0.00	0.46	0.47	0.00	0.60	0.00	0.00	0.35	0.00
FeO	2.08	2.78	6.10	6.42	6.96	6.54	1.66	2.99	4.79	2.10
MnO	0.22	0.18	0.20	0.25	0.19	0.27	0.18	0.16	0.12	0.21
MgO	15.07	14.65	13.42	13.18	12.87	12.81	14.57	14.77	14.52	15.00
CaO	22.81	22.50	23.50	23.04	23.03	23.10	22.30	22.98	24.01	22.66
Na_2O	1.37	1.46	0.89	1.00	0.97	1.09	1.85	1.20	0.68	1.40
Total	98.47	98.30	98.98	98.72	98.25	98.82	97.97	98.48	99.23	98.91
Apfu normalized to 6 oxygen atoms										
Si	1.89	1.94	1.98	1.98	1.99	1.98	1.92	1.94	1.98	1.90
Al	0.07	0.05	0.01	0.01	0.01	0.01	0.06	0.03	0.01	0.06
T site	1.96	1.98	1.99	1.99	2.00	1.99	1.97	1.98	1.99	1.95
Ti	0.12	0.10	0.04	0.04	0.04	0.05	0.13	0.09	0.04	0.14
Cr	0.00	0.01	0.00	0.00	0.00	0.00	0.01	0.00	0.00	0.00
Fe^{3+}	0.00	0.00	0.01	0.01	0.00	0.02	0.00	0.00	0.01	0.00
Fe^{2+}	0.06	0.09	0.19	0.20	0.22	0.21	0.05	0.09	0.15	0.07
Mg	0.81	0.81	0.75	0.74	0.73	0.72	0.81	0.81	0.81	0.79
Mn	0.00	0.00	0.01	0.00	0.01	0.01	0.00	0.00	0.00	0.00
M2 site	1.00	1.00	1.00	1.00	1.00	1.00	1.00	1.00	1.00	1.00
Mn	0.01	0.01	0.00	0.01	0.00	0.00	0.01	0.01	0.00	0.01
Mg	0.02	0.01	0.00	0.00	0.00	0.00	0.00	0.01	0.00	0.03
Ca	0.91	0.90	0.94	0.93	0.93	0.93	0.89	0.92	0.96	0.90
Na	0.10	0.11	0.06	0.07	0.07	0.08	0.13	0.09	0.05	0.10
M1 site	1.03	1.02	1.01	1.01	1.00	1.01	1.03	1.02	1.01	1.04
Wo	50.16	49.95	49.73	49.32	49.66	49.74	50.83	50.10	49.81	50.17
En	46.10	45.23	39.52	39.24	38.62	38.37	46.22	44.81	41.92	46.21
Fs	3.73	4.82	10.76	11.43	11.71	11.90	2.95	5.09	8.27	3.62

Table 2. Representative EMPA data of clinopyroxene.

manganese field, South Africa (ICDD database entry no. 87-1971–12.340(1) Å)[49], San Benito, California, the USA (ICDD database entry no. 84-2015–12.105(3) Å)[4] (Table 6; for more details see Table 1S) or synthetic species (a = 12.5424(5) Å and 12.4297(7) Å[3].

Discussion

The hydrous, titanian andradite occurs in close paragenesis with clinochlore, calcite, blue pectolite, prehnite, and natrolite. It is also associated with palagonitized glass (mixture of chlorite, trioctahedral smectite, and trioctahedral illite), and opaque minerals such as magnetite, ilmenite, rutile, titanite, and manganite, all found within strongly altered pyroclastic material. The presence of prehnite, pumpellyite, natrolite, and clinochlore is consistent with zeolite, prehnite-pumpellyite metamorphic facies. The mineral assemblage was formed during seafloor hydrothermal alterations[32]. Natrolite often coexists with blue pectolite and calcite. While natrolite had surely formed in an aluminum-rich environment, pectolite crystallized later when the Al content decreased in the fluids[50]. The experiments conducted by Chen et al.[51] demonstrated that carbonate precipitates prior to pectolite within the temperature range of 150–210 °C. Consequently, Huang et al.[50] proposed that a probable sequence of crystallization in the Filipinas mine is natrolite ◊ calcite ◊ pectolite. Finally, the palagonitized glass is believed to have been formed during the latest stage of rocks evolution under hypergenic conditions.

In the studied samples the hydrous andradite, which forms small, euhedral grains loosely distributed in the chloritized groundmass of lithoclasts (first textural type) is the most abundant in the rocks. It probably crystallized after the groundmass of lithic elements of pyroclastic rocks. The second type, forming veins and layers infillings, found in paragenesis with chlorite, was formed due to the alteration of vitroclasts. Eventually, the morphological features of the third textural type of hydrous andradite, i.e. polycrystalline aggregates found within the tabular forms, most probably represent the pseudomorphs after primary magmatic phases, such as Ca feldspars and Ca clinopyroxenes, though no relics of these phases are found within the garnets (Fig. 12). Metasomatism involving Ca^{2+}, Na^{+}, Fe^{2+} aqueous fluids was a key driving force to the garnetization of the pyroclastic rocks from the Sierra de Bahoruco area. The strong large-scale Ca-metasomatic event that occurred in the late stages of the evolution of the Dumisseau Formation was extensively discussed by Escuder-Viruete et al.[32] and Wachowiak et al.[34]. In the first stage, it is likely that Ca plagioclase forming both crystaloclasts

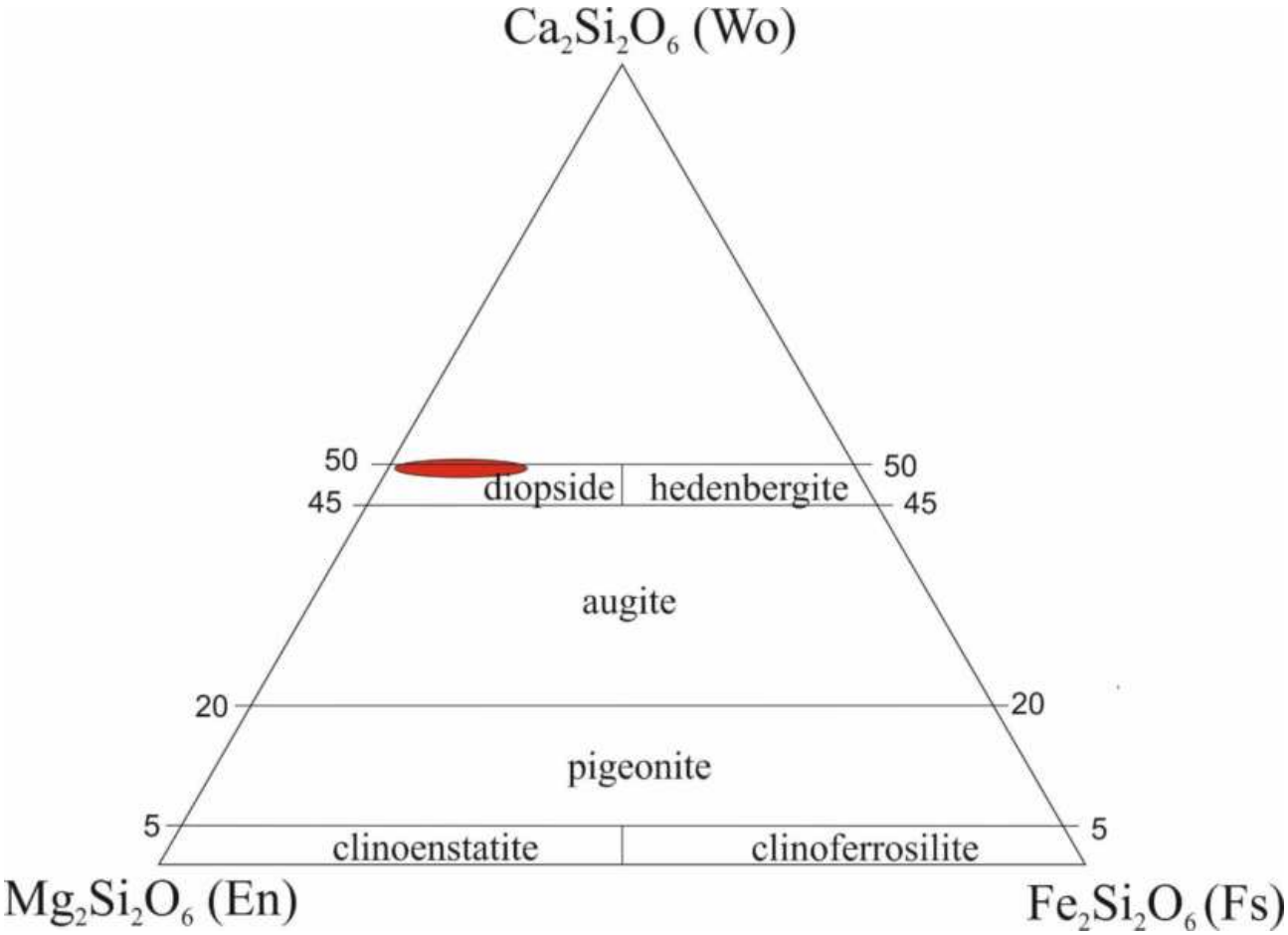

Fig. 8. The composition of clinopyroxene plotted on a wollastonite ($Ca_2Si_2O_6$) - Enstatite ($Mg_2Si_2O_6$) - Ferrosilite ($Fe^{2+}{}_2Si_2O_6$) triangular diagram[37].

or components of lithoclasts[34] was transformed into hydrous garnets (third textural type). Along with the evolution of metasomatic transformations of the pyroclastic rocks, both vitroclasts and cryptocrystalline or aphanitic groundmass of lithoclasts were altered to Fe^{2+}-depleted chlorite (clinochlore). At the same time, or subsequently, some prisms of strongly chloritized clinopyroxenes were also pervasively replaced by hydrous garnets. Subsequently, hydrous andradite forming both individual grains (first textural type) within chlorite and infillings of veins (second textural type) was formed in the studied rocks.

Regardless of the textural type of hydrous garnet, all species have quite a homogeneous composition. Only the garnet of the first textural type shows chemical zoning and displays the distinct increase in Fe^{2+} towards the core zones. These slight differences in composition imply the central domain of this species crystallized when the activity of Fe^{2+} in the mineralizing solutions was higher than when the other hydrous andradite formed. The main hydrous garnet-forming elements (i.e., Ca^{2+}, Fe^{3+}, and Si) could have been released via subsequent alteration of magmatic phases, such as clinopyroxene (diopside, Ca feldspars) and volcanic groundmass. Calcium from the rocks could be mobilized under relatively low-temperature conditions. Hara and Tsuchiya[52] examined hydrothermal water–pyroclastic rock interactions using flow-through experiments and concluded that Ca was selectively depleted from the rock surface at temperatures below 150 °C, whereas other elements such as Na were leached at higher temperature conditions. Some amounts of Ca, needed for the formation of secondary garnet, could be mobilized also from an external source, i.e. country rock (i.e., limestones) overlying the volcanic rocks of the Sierra de Bahoruco area). In the Miocene-Pliocene, the Sierra de Bahoruco region was affected by strong tectonic movements[32], which created the migration paths for Ca-bearing fluid within the volcanic rocks.

In the presence of low-temperature fluids, numerous factors may have contributed to the stability of andradite[9,53]. These include: (1) low silica activity to stabilise andradite relative to other Ca-Fe phases, (2) low CO_2 activity to prevent deposition of calcite, and (3) high Ca activity and relatively high fluid-pH to stabilise andradite relative to iron oxide phases. These constraints posit that hydrous andradite formed at the latest stage of Ca metasomatism when the fluids were depleted in SiO_2 and CO_2, but still Ca-rich.

In general, the hydrogen content decreases with temperature, resulting in more hydrous garnets formed under lower temperature conditions[2,54]. Amthauer and Rossman[2] analysed the content of water in garnets originating from various geological settings using Fourier transform IR spectroscopy. They noted that hydrous andradite from cavities in basalts (Bombay, India), formed under low-temperature and low-pressure postmagmatic

Analytical points	H1_4	H1_5	H1_8	H1_13	H1_14	H1_15	H1_18	H1_19	H1_20	H1_21	H1_22	H1_23	H1_24	H1_25
Composition (wt.%)														
SiO_2	32.89	32.68	33.05	31.42	31.07	31.40	30.77	30.96	32.18	30.98	31.58	31.66	31.54	32.33
TiO2	0.00	0.00	0.00	0.00	0.00	0.00	0.00	0.71	0.07	0.32	0.00	0.00	0.00	0.00
Al_2O_3	12.55	12.54	12.74	9.30	9.95	9.55	9.10	8.78	10.46	10.14	9.92	9.92	10.68	10.44
Cr_2O_3	0.00	0.00	0.06	0.00	0.00	0.00	0.00	0.00	0.00	0.00	0.00	0.00	0.00	0.00
FeO	13.36	12.86	12.76	20.87	19.50	19.35	20.33	20.62	18.66	18.69	19.71	18.59	16.88	17.49
MnO	0.46	0.43	0.46	0.21	0.24	0.22	0.19	0.14	0.23	0.22	0.20	0.27	0.21	0.23
MgO	25.10	25.48	24.57	23.88	23.64	25.01	24.32	24.03	24.09	24.80	24.06	23.91	25.25	24.73
CaO	0.72	0.70	0.72	0.28	0.29	0.24	0.25	0.73	0.44	0.49	0.39	0.86	0.26	0.32
Na_2O	0.11	0.13	0.13	0.00	0.00	0.00	0.00	0.00	0.00	0.00	0.00	0.14	0.00	0.00
K_2O	0.41	0.30	0.29	0.00	0.00	0.28	0.00	0.00	0.00	0.00	0.00	0.00	0.00	0.00
H_2O (*calc.*)	11.83	11.80	11.78	11.47	11.34	11.55	11.38	11.40	11.58	11.51	11.49	11.42	11.52	11.58
Totals	97.44	96.91	96.55	97.44	96.02	97.58	96.36	97.37	97.69	97.15	97.33	96.77	96.34	97.10
apfu based on 14 oxygen equivalents														
Si	3.33	3.32	3.37	3.29	3.29	3.26	3.24	3.26	3.33	3.23	3.30	3.32	3.28	3.35
Al^{IV}	0.67	0.68	0.63	0.71	0.71	0.74	0.76	0.74	0.67	0.77	0.70	0.68	0.72	0.65
Al^{VI}	0.83	0.82	0.90	0.43	0.53	0.43	0.37	0.35	0.61	0.47	0.52	0.55	0.59	0.62
Ti	0.00	0.00	0.00	0.00	0.00	0.00	0.00	0.06	0.01	0.03	0.00	0.00	0.00	0.00
Cr	0.00	0.00	0.01	0.00	0.00	0.00	0.00	0.00	0.00	0.00	0.00	0.00	0.00	0.00
Fe^{3+}	0.00	0.00	0.00	0.22	0.12	0.22	0.33	0.12	0.00	0.14	0.10	0.00	0.07	0.00
Fe^{2+}	1.13	1.09	1.09	1.61	1.60	1.46	1.46	1.70	1.62	1.49	1.62	1.63	1.40	1.52
Mn	0.04	0.04	0.04	0.02	0.02	0.02	0.02	0.01	0.02	0.02	0.02	0.02	0.02	0.02
Mg	3.79	3.86	3.73	3.72	3.73	3.87	3.82	3.77	3.72	3.85	3.74	3.74	3.92	3.82
Σ Octahedral cations	5.80	5.82	5.76	6.00	6.00	6.00	6.00	6.00	5.97	6.00	6.00	5.95	6.00	5.98
□	0.20	0.18	0.24	0.00	0.00	0.00	0.00	0.00	0.03	0.00	0.00	0.05	0.00	0.02
Ca	0.0786	0.08	0.08	0.03	0.03	0.03	0.03	0.08	0.05	0.05	0.04	0.10	0.03	0.04
Na	0.0214	0.03	0.02	0.00	0.00	0.00	0.00	0.00	0.00	0.00	0.00	0.03	0.00	0.00
K	0.0529	0.04	0.04	0.00	0.00	0.04	0.00	0.00	0.00	0.00	0.00	0.00	0.00	0.00
Σ Interlayer cations	0.15	0.14	0.14	0.03	0.03	0.06	0.03	0.08	0.05	0.05	0.04	0.13	0.03	0.04
R^{2+}	4.97	4.99	4.86	5.35	5.35	5.35	5.30	5.48	5.36	5.36	5.38	5.40	5.34	5.35
Mg#	0.77	0.78	0.77	0.70	0.70	0.73	0.72	0.69	0.70	0.72	0.70	0.70	0.74	0.72
Temperature [°C][24]	152	156	142	168	168	176	182	177	153	187	164	156	169	148
Temperature [°C][25]	155	157	148	165	165	170	174	171	155	177	163	157	165	152

Table 3. Representative EMPA data of chlorite.

conditions, had the highest H_2O content (6 wt%) of all garnets of their study. The water content calculated from stoichiometry in our study (2.00–4.00 apfu OH) indicates the garnets had to be stable below 450 °C and 300 °C, respectively[54,55]. These results are consistent with those obtained from chlorite geothermometry (140–187 °C). In addition to low temperatures, the incorporation of OH^- in hydrous garnet from the Dominican Republic was also facilitated by the presence of structural defects resulting from the complex crystal chemistry, specifically a slight Si deficiency, and distribution of Ti, Al and Fe over octahedral sites[2]. The OH incorporation was probably necessary to achieve a charge balance of the species.

Concluding remarks

1. Titanium-bearing, hydrous andradite with average formula $[Ca_{2.98}Na_{0.02}K_{0.01}Fe^{2+}{}_{0.01}][Fe^{3+}{}_{1.25}Al_{0.45}Ti_{0.15}Fe^{2+}{}_{0.07}Mg_{0.04}V^{3+}{}_{0.01}Mn^{2+}{}_{0.01}]Si_{2.43}O_{9.72}(OH)_{2.28}$ occurs abundantly within pyroclastic rocks of the Sierra de Bahoruco region in the Dominican Republic. It is primarily found in close paragenesis with clinochlore and calcite, but also prehnite, pectolite, and natrolite.
2. The crystal structure of hydrous andradite from pyroclastic rocks of the Sierra de Bahoruco area is more similar to hydrous grossular and morimotoite than hydrous andradite from different localities worldwide. This is probably due to the elevated titanium (up to 3.71 wt% TiO_2) and aluminum (up to 9.3 2 wt% Al_2O_3) contents in its structure.
3. Hydrous andradite is a secondary mineral that formed under a low-temperature, pervasive, calcic metasomatic event related to the interaction of high-pH hydrothermal fluids with magmatic components of pyroclastic rocks under oxidizing conditions.

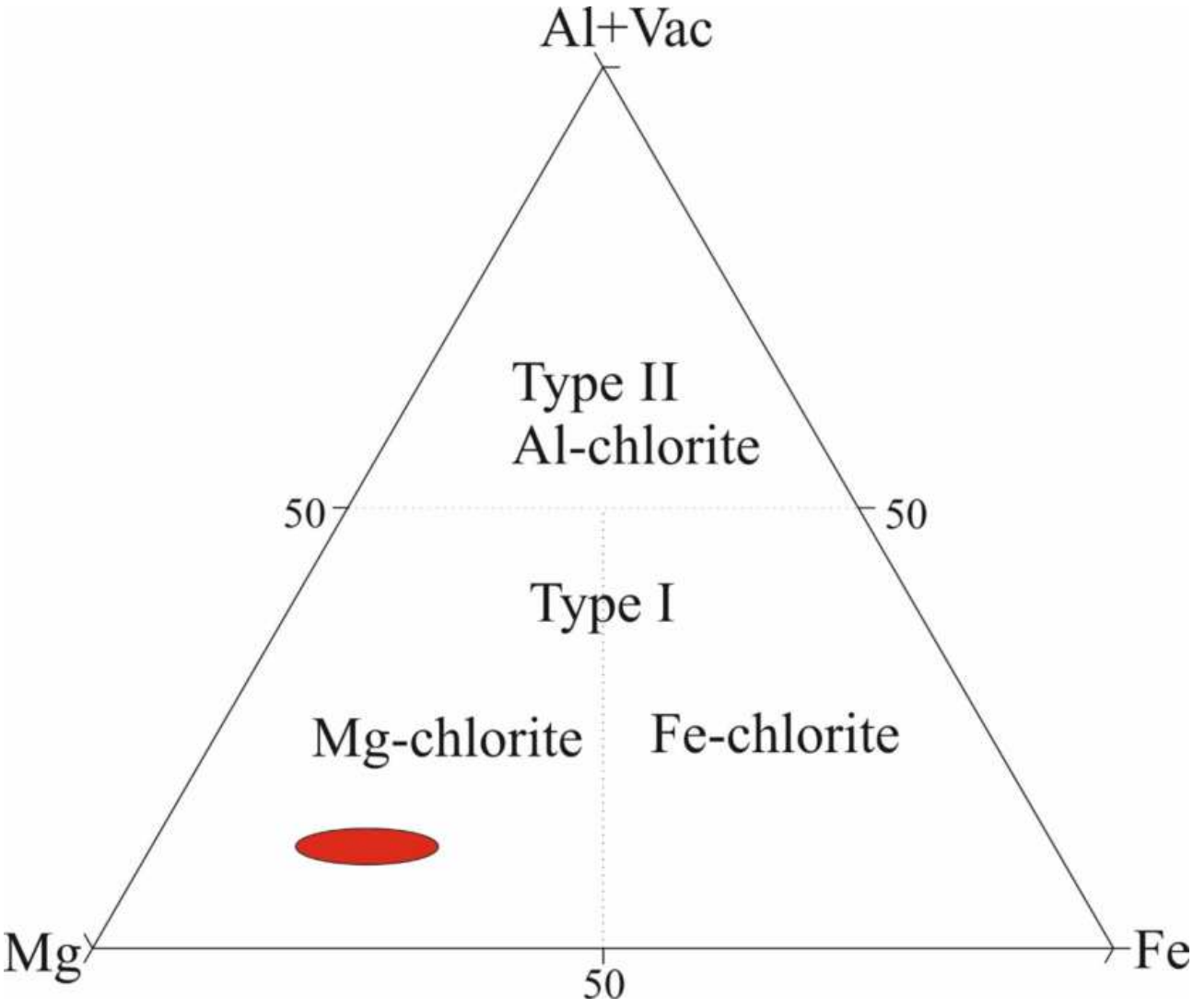

Fig. 9. The composition of chlorite plotted on triangular Al + Vac–Mg–Fe compositional classification diagram[38].

Sampling and analytical methods

From the abundant analytical material, brought during three expeditions to the Dominican Republic (2013, 2016, and 2019), the representative rock samples were selected for the detailed examination. The pyroclastic rocks bearing hydrous garnets were collected in the active Las Filipinas larimar mine with well-exposed Cretaceous-Tertiary lithologies (Fig. 1C).

Polarizing microscopy

Preliminary observations of the pyroclastic rocks were carried out using a stereoscopic microscope type SNZ-168, coupled with a digital camera (0.75×, 1×, 2×, 3×, 4×, and 5× objectives) and equipped with the Panasis computer software.

The polished thin sections of the rock samples hosting hydrous garnets were observed using an Olympus BX 51 polarizing microscope under both transmitted and reflected light (in a magnification range from 40 to 400 times). The microphotographs were taken using an Olympus DP12 digital camera linked to Analysis software.

Scanning electron microscopy coupled with energy-dispersive X-ray spectrometry (SEM-EDS)

Textural relationships of the pyroclastic rocks from Las Filipinas larimar mine were described using a FEI Quanta 200 FEG scanning electron microscope equipped with an energy dispersive spectrometer (EDS). The system operated in the low-vacuum mode (pressure of 60 Pa, the samples were not coated) at maximum excitation voltage of 20 kV. The quantitative analyses of target elements, based on relative peak intensity calculated from the EDS spectrum, were supported by ZAF correction.

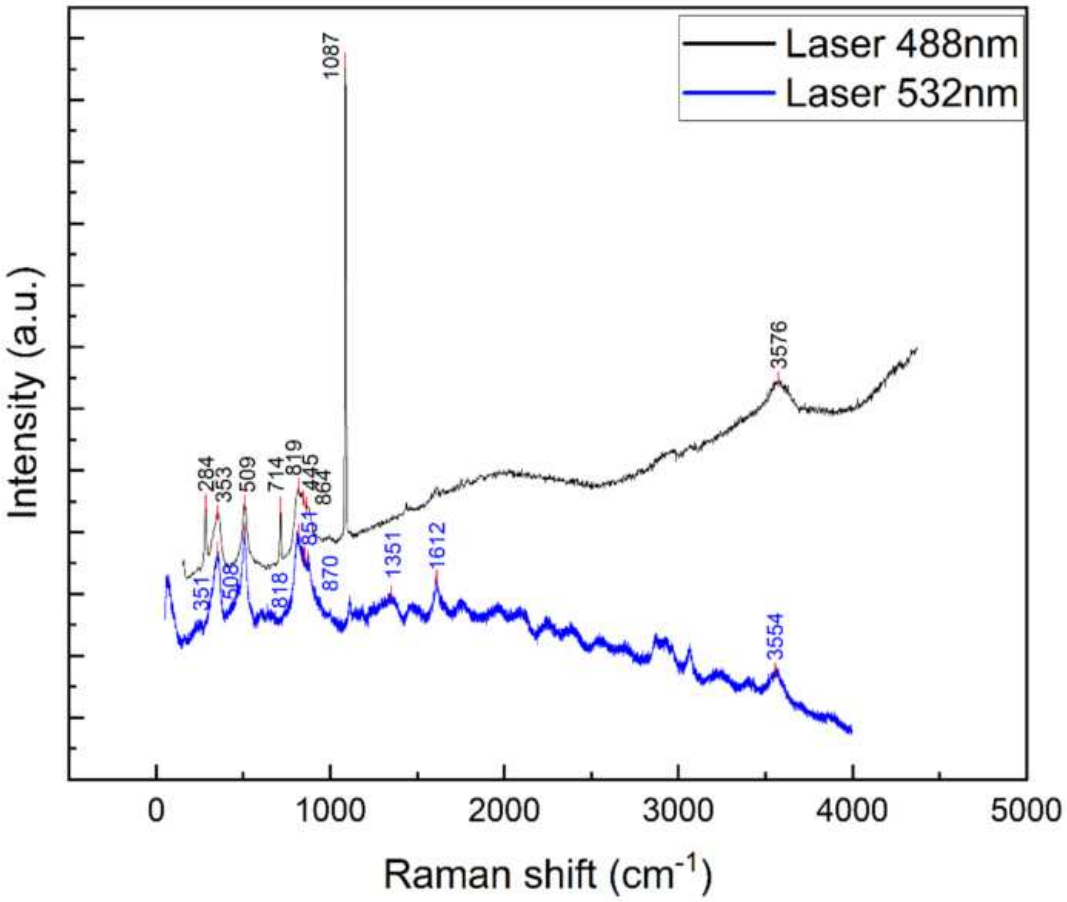

Fig. 10. Raman spectra of hydrous garnet in the range 0–4500 cm^{-1} (excitation 488 and 532 nm).

Raman bands (488 nm laser)	Raman bands (532 nm laser)	Assignment (Jehlicka et al. 2009)[44]
157	160	Translation of [SiO_4] tetrahedron (Jehlicka et al. 2009)[44]
240	245	Translational of X^{2+} dodecahedral cations (Jehlicka et al. 2009)[44]
353	353	Rotation of [SiO_4] tetrahedra (Jehlicka et al. 2009)[44]
509	508	Si-O bending (Jehlicka et al. 2009)[44]
819	818	Si-O stretching (Jehlicka et al. 2009)[44]
845	851	
864	870	
995	999	
3576	3554	OH stretching[9,13]

Table 4. Raman band positions and their assignment for hydrous andradite (488 and 532 nm excitation lines).

Electron probe micro-analysis (EPMA)

Microchemical analyses of hydrous garnets, coexisting chlorite, and relics of pyroxene were carried out with the JEOL JXA-8320 electron microprobe located at the AGH-KGHM Laboratory of Critical Elements in AGH University of Krakow, Poland. The system operated in a wavelength-dispersive (WDS) mode under the following conditions: acceleration voltage 15 kV, probe current 20nA, beam diameter 1–3 µm, peak counting time 20 s, and background counting time 10 s for each offset position. The EMPA standards, analytical lines, diffracting crystals, and mean detection limits for particular elements analyzed in all species are presented in Table 7. The

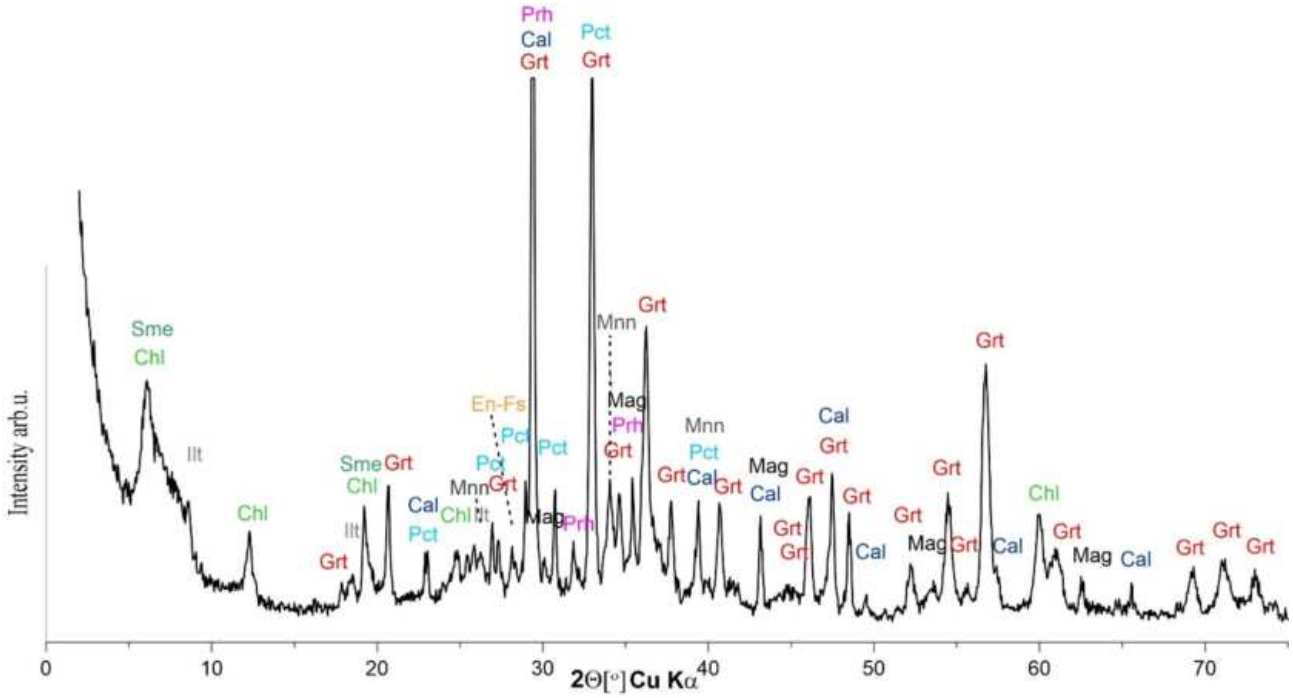

Fig. 11. XRD pattern of garnet rich fraction selected from pyroclastic material from the Las Filipinas larimar mine. Grt – Garnet (47-1877, 33–285), Cal – Calcite (05-0586), Pct – Pectolite (74-1109), Chl – Chlorite (16–0362), Sme – Smectite, Ilt – Illite, Mnn – Manganite (41-1379), Mag – Magnetite (19–0629), Prh – Prehnite (29–0290), En-Fs – Enstatite (19–768)- ferrosilite (29–721). In brackets, the ICDD database entry numbers are given.

h	k	l	d_{cal} [Å]	d_{obs} [Å]
2	2	0	4.3033	4.3047
4	2	0	2.7217	2.7247
3	3	2	2.5950	2.5928
4	2	2	2.4845	2.4845
5	1	0	2.3871	2.3869
5	2	1	2.2222	2.2224
5	3	2	1.9745	1.9752
6	4	0	1.6879	1.6885
10	4	0	1.1301	1.1300

Table 5. The assigned reflections of garnet for calculation of unit cell parameter.

raw data was corrected with the ZAF analytical procedure. The calculations of the Fe^{2+}/Fe^{3+} ratio and the OH^- group content in the garnet chemical formulas were based on the charge balance and were made according to the recommendations of Grew et al.[1]. The crystal-chemical formula of pyroxene was calculated based on 6 oxygen atoms. The calculation and classification of chlorite were done using a Windows program (WinCcac) by Yavuz et al.[56]. The temperature of chlorite formation was calculated using two independent geothermometers based on Al (apfu) content i.e.: (1) T (°C) = 106 · $Al^{IV}(O_{28})$ + 18[25]; (2) T (°C) = −61.92 + 160.99 · $Al^{IV}(O_{28})$[24]. Other semi-empirical and graphical approaches based on the contents of silica, Fe/(Fe + Mg), and the sum of divalent cations (R^{2+}) were abandoned due to the inability to determine the exact Fe^{2+}/Fe^{3+} ratio. Moreover, the presence of traces of Ca + Na + K and high Si may suggest some contamination of chlorite with other phases, e.g. calcite and/or the interstratified chlorite-smectite phases[42].

Raman microspectroscopy

Raman spectra of garnets were collected using two Raman spectrometers: (1) LabRAM HR UV-Vis-NIR (200–1600 nm) with 532 nm laser equipped with Olympus BX-41 optical microscope and (2) the Witec Alpha

Garnet species	Chemical Formula	Space group/cell parameter [Å]
Hydrous garnet from Dominican Republic – this study	$[Ca_{2.98}Na_{0.02}K_{0.01}Fe^{2+}{}_{0.01}][Fe^{3+}{}_{1.25}Al_{0.45}Ti_{0.15}Fe^{2+}{}_{0.07}Mg_{0.04}V^{3+}{}_{0.01}Mn^{2+}{}_{0.01}]\ Si_{2.43}O_{9.72}(OH)_{2.28}$	Space Group: Ia-3d Cell a: 12.172(5)
Hydrogrosular (Hibschite) Crestmore, USA (ICDD no 75-169)[48]	$Ca_{3.0}Al_{2.0}(SiO_4)_{1.53}(OH)_{5.88}$	Space Group: Ia-3d Cell a: 12.174
Morimotoite Fuca. Ocayama. Japan. (ICDD no 47-1877)[47]	$Ca_{3.0}TiFeSi_{3.0}O_{12.0}$	Space Group: Ia-3d Cell a: 12.162(3)
Schörlomite San Benito, Ca, USA. (ICDD no 33-0285) (Krabbenhoft and McCarthy 1980)	$Ca_{3.0}\ (Ti, Fe)_{2.0}[(Si, Ti)O_{4.0}]_{3.0}$	Space Group: Ia-3d Cell a: 12.128
Hydrous Andradite South Africa (ICDD no 87-1971)[49]	$Ca_{3.0}Fe_{1.54}Mn_{0.2}\ Al_{0.26}(SiO_4)_{1.65}(OH)_{5.40}$	Space Group: Ia-3d Cell a: 12.340(1)
Andradite San Benito, Ca, USA (ICDD no 84-2015)[4]	$Ca_{3.0}\ Fe_{1.6}\ Al_{0.4}(SiO_4)_{2.58}(OH)_{1.68}$	Space Group: Ia-3d Cell. a: 12.105(3)

Table 6. The chemistry and crystal structure data of hydrous andradite from pyroclastic rocks of Siera De Bahoruco compared with literature data of other garnet species worldwide.

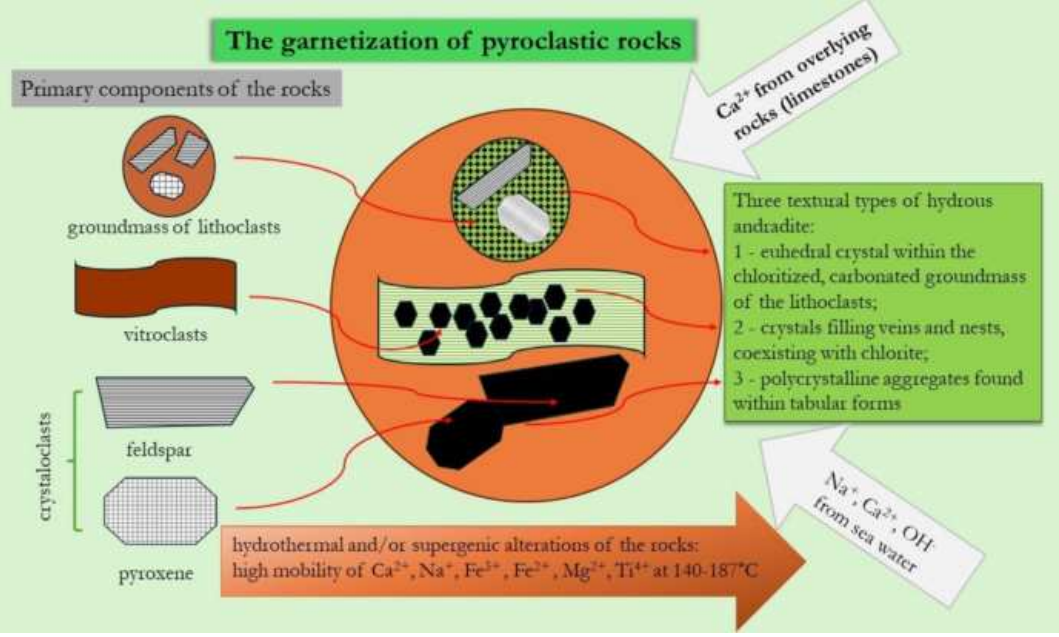

Fig. 12. The simplified model of hydrous andradite formation within the pyroclastic rocks from Las Filipinas larimar mine in the Dominican Republic.

300 M + with 488 nm laser line equipped with Zeiss optical microscope. Both spectrometers are located at the Department of Silicate Chemistry and Macromolecular Compounds, Faculty of Materials Science and Ceramics, AGH University of Krakow. The spectra were corrected for background by the sextic polynomial method using Omnic software.

X-Ray powder diffraction (XRPD)

The X-ray diffractometry studies were performed on powdered garnet-rich fraction, separated manually from the rock samples under the stereoscopic microscope. The identification of clay minerals in the sample was made based on XRPD patterns of samples under air-dry, calcinated, and ethylene-glycol-saturated conditions. The XRPD analyses were carried out using a Rigaku Smart Lab 9.0 kW diffractometer with reflective graphite-monochromatized CuKα radiation. The diffraction data were collected in the angular range of 3–75 °2θ with a step size of 0.02° and a counting time of 2 s/step at a voltage of 45 kV and a current of 200 mA with a pure halite crystal used as an internal standard. The XRPD pattern was evaluated by XRAYAN software using a diffraction pattern database (Powder Diffraction File PDF-2) of the International Centre for Diffraction Data (2018). The

hydrogarnet					chlorite					pyroxene				
Element	Signal	WDS crystal	Standard	Detection limit (ppm)	Element	Signal	WDS crystal	Standard	Detection limit (ppm)	Element	Signal	WDS crystal	Standard	Detection limit (ppm)
P	Kα	PETJ	YPO_4		Si	Kα	TAP	Albite	300	Si	Kα	TAP	Albite	300
Si	Kα	TAP	Albite		Al	Kα	TAPH	Albite	350	Al	Kα	TAPH	Albite	320
Al	Kα	TAPH	Albite		Cr	Kα	LIFL	Chromite	350	Ti	Kα	PETJ	Rutile	300
Ti	Kα	PETJ	Rutile		Fe	Kα	LIFH	Hematite	300	Fe	Kα	LIFL	Hematite	300
Cr	Kα	LIF	Cr_2O_3,		Mn	Kα	LIF	Rhodonite	500	Mg	Kα	TAP	Diopside	230
V	Kα	LIF	Vanadium		Mg	Kα	TAP	Diopside	220	Ca	Kα	PETL	Diopside	100
Fe	Kα	LIFL	Fayalite		Ca	Kα	PETL	Diopside	100	Na	Kα	TAPH	Albite	230
Mn	Kα	LIF	Rhodonite		Na	Kα	TAPH	Albite	250	K	Kα	PETJ	Sanidine	150
Mg	Kα	TAP	Diopside		K	Kα	PETJ	Sanidine	170					
Ca	Kα	PETL	Diopside											
Na	Kα	TAPH	Albite											
K	Kα	PETJ	Sanidine											
F	Kα	TAP	Fluorite											

Table 7. The operating conditions of EMPA analyses of pectolite, pyroxene, and chlorite.

garnet unit cell parameters were refined for the cubic space group *Ia-3d* following the data of the ICDD database (entry no 47-1877). The calculation was based on nine reflections of garnet that did not overlap with reflections of other components of the sample.

Data availability

Data is provided within the manuscript and supplementary information file.

Received: 29 March 2024; Accepted: 26 November 2024
Published online: 02 December 2024

References

1. Grew, E. S. et al. IMA report: nomenclature of the garnet supergroup. *Am. Mineral.* **98**, 785–810 (2013).
2. Amthauer, G. & Rossman, G. R. The hydrous component in andradite garnet. *Am. Mineral.* **83**, 835–840 (1998).
3. Dilnesa, B. Z., Lothenbach, B., Renaudin, G., Wichser, A. & Kulik, D. Synthesis and characterization of hydrogarnet $Ca_3(Al_xFe_{1-x})_2(SiO_4)_y(OH)_{4(3-y)}$. *Cem. Concr Res.* **59**, 96–111 (2014).
4. Lager, G. A., Armbruster, T., Rotella, F. J. & Rossman, G. R. OH substitution in garnets: X-ray and neutron diffraction, infrared, and geometric-modeling studies. *Am. Mineral.* **74**, 840–851 (1989).
5. Passaglia, E. & Rinaldi, R. A new nomenclature for the hydrogrossular group of minerals. *Bull. MinÃ©ral.* **107**, 605–618 (1984).
6. Albrecht, R., Doert, T. & Ruck, M. The hydrogarnets $Sr_3[RE(OH)_6]_2$ (RE = sc, Y, Ho – Lu): syntheses, crystal structures, and their thermal decomposition to ternary rare-earth metal oxides. *Z. Anorg Allg Chem.* **646**, 1517–1524 (2020).
7. Deer, W. A., Howie, R. A. & Zussman, J. *An Introduction to the Rock-Forming Minerals* (The Mineralogical Society, 2013).
8. Duraj, M., Marschalko, M., Duda, R., Sitányiová, D. & Masarovičová, S. The history of pyrope extraction and processing in the Czech Republic and its significance for geotourism. *Procedia Earth Planet. Sci.* **15**, 663–668 (2015).
9. Ghosh, B. et al. A new occurrence of titanian (hydro)andradite from the Nagaland ophiolite, India: implications for element mobility in hydrothermal environments. *Chem. Geol.* **457**, 47–60 (2017).
10. Onuki, H., Akasaka, M., Yoshida, T. & Nedachi, M. Ti-rich hydroandradites from the Sanbagawa metamorphic rocks of the Shibukawa Area, Central Japan. *Contribution Mineralogy Petrol.* **80**, 183–188 (1982).
11. Peters, T. A water-bearing andradite from the Totalp serpentinite (Davos, Switzerland). *Am. Mineral.* **50**, 1482–1486 (1965).
12. Ford, R. J. A hydrogarnet from Tasmania. *Mineral. Mag.* **37**, 942–943 (1970).
13. Schmitt, A. C., Tokuda, M., Yoshiasa, A. & Nishiyama, T. Titanian andradite in the Nomo rodingite: Chemistry, crystallography, and reaction relations. *J. Mineral. Petrol. Sci.* **114**, 111–121 (2019).
14. Salvioli-Mariani, E. et al. Multi-stage rodingitization of ophiolitic bodies from Northern Apennines (Italy): constraints from petrography, geochemistry and thermodynamic modelling. *Geosci. Front.* **11**, 2103–2125 (2020).
15. Li, X. P. et al. Rodingites from the Xigaze ophiolite, southern Tibet – new insights into the processes of rodingitization. *Eur. J. Mineral.* **29**, 821–837 (2017).
16. Basso, R., Cimmino, F. & Messiga, B. Crystal chemical and petrological study of hydrogarnets from a Fe-gabbro metarodingite (Gruppo Di Voltri, Western Liguria, Italy). *Neues Jahrbuch für Mineralogie Abhandlungen*. **150**, 247–258 (1984).
17. Alavi, G., Radmard, K., Zamanian, H., Hosseinzadeh, M. R. & Khalaji, A. A. Geochemistry of skarn and porphyry deposits in relation to epithermal mineralization in the arasbaran metallogenic zone, NE Tabriz, Iran. *Geol. Q.* **64**, 141–164 (2020).
18. Flohr, M. J. K. & Ross, M. Alkaline igneous rocks of Magnet Cove, Arkansas: Metasomatized Ijolite xenoliths from Diamond Jo quarry. *Am. Mineral.* **7**, 113–131 (1989).
19. Farré-de-Pablo, J. et al. Low-temperature hydrothermal pt mineralization in uvarovite-bearing ophiolitic chromitites from the Dominican Republic. *Min. Depos.* **57**, 955–976 (2022).
20. Proenza, J., Sole, J. & Melgarejo, J. C. Uvarovite in podiform chromitite: the Moa-Baracoa ophiolitic Massif, Cuba. *Can. Mineral.* **37**, 679–690 (1999).
21. Jenkins, L. E., Lee, M. R., Daly, L., King, A. J. & Li, S. Calc-silicate metasomatism in CM chondrites Shidian and Kolang: The First Report of Asteroidal Hydroandradite. In *53rd Lunar and Planetary Science Conference* Vol. 2678, 1515 (2022).
22. Dumańska-Słowik, M. et al. Origin of bluish pectolite aka larimar from the Dominican Republic: constraints from mineralogy and geochemistry. *J. South. Am. Earth Sci.* **141**, (2024).
23. Vidal, O., Lanari, P., Munoz, M., Bourdelle, F. & De Andrade, V. Deciphering temperature, pressure and oxygen-activity conditions of chlorite formation. *Clay Min.* **51**, 615–633 (2016).
24. Cathelineau, M. Cation site occupancy in chlorites and illites as a function of temperature. *Clay Min.* **23**, 471–485 (1988).
25. Cathelineau, M. & Nieva, D. A chlorite solid solution geothermometer the Los Azufres (Mexico) geothermal system. *Contrib. Miner. Petrol.* **91**, 235–244 (1985).
26. Lapierre, H. et al. Late jurassic oceanic crust and upper cretaceous Caribbean plateau picritic basalts exposed in the Duarte igneous complex, Hispaniola. *J. Geol.* **107**, 193–207 (1999).
27. Escuder Viruete, J. et al. Tectónica Y geoquímica De La formación Amina: Registro Del Arco Isla Caribeño primitivo en la Cordillera Central, República Dominicana. *Bol. Geol. y Min.* **118**, 221–242 (2007).
28. Loewen, M. W., Duncan, R. A., Kent, A. J. R. & Krawl, K. Prolonged plume volcanism in the Caribbean large Igneous Province: new insights from Curaçao and Haiti. *Geochem. Geophys. Geosyst.* **14**, 4241–4259 (2013).
29. Whattam, S. A. & Stern, R. J. Late cretaceous plume-induced subduction initiation along the southern margin of the Caribbean and NW South America: the first documented example with implications for the onset of plate tectonics. *Gondwana Res.* **27**, 38–63 (2015).
30. Sen, G., Hickey-Vargas, R., Waggoner, D. G. & Maurrasse, F. Geochemistry of basalts from the Dumisseau Formation, southern Haiti: implications for the origin of the Caribbean Sea crust. *Earth Planet. Sci. Lett.* **87**, 423–437 (1988).
31. Escuder-Viruete, J., Pérez-Estaún, A. & Weis, D. Geochemical constraints on the origin of the late jurassic proto-caribbean oceanic crust in Hispaniola. *Int. J. Earth Sci.* **98**, 407–425 (2009).
32. Escuder-Viruete, J., Joubert, M., Abad, M., Pérez-Valera, F. & Gabites, J. The basaltic volcanism of the Dumisseau formation in the Sierra De Bahoruco, SW Dominican Republic: a record of the mantle plume-related magmatism of the caribbean large Igneous Province. *Lithos* **254–255**, 67–83 (2016).
33. Wagner, M. et al. Petrographic and mineralogical studies of fossil charcoal from Sierra De Bahoruco (Barahona Province, Dominican Republic). *Int. J. Coal Geol.* **173**, 142–149 (2017).
34. Wachowiak, J., Natkaniec-Nowak, L., Rodriguez, J., Heflik, W. & George, C. Contribution to the knowledge of the rocks hosting the blue pectolite (larimar) deposit in the SW part of the Dominican Republic. *Neues Jahrb Geol. Palaontol Abh*. **303**, 257–270 (2022).
35. Bačík, P. et al. Vanadian and chromian garnet- and epidote-supergroup minerals in metamorphosed paleozoic black shales from Čierna Lehota, Strážovské Vrchy Mountains, Slovakia: crystal chemistry and evolution. *Mineral. Mag.* **82**, 889–911 (2018).
36. Liang, P., Zhang, Y. & Xie, Y. Chemical composition and genesis implication of garnet from the Laoshankou Fe-Cu-Au deposit, the Northern Margin of East Junggar, NW CHina. *Minerals* **11**, (2021).

37. Morimoto, N. et al. Nomenclature of pyroxenes Subcommittee on Pyroxenes Commission on New Minerals and Mineral Names International Mineralogical Association. *Am. Mineral.* **73**, 1123–1133 (1988).
38. Zane, A. & Weiss, Z. A procedure for classifying rock-forming chlorites based on microprobe data. *Rend. Lincei Sci. Fis. Nat.* **9**, 51–55 (1998).
39. de Caritat, P., Hutcheon, I. & Walshe, J. L. Chlorite geothermometry: a review. *Clays Clay Min.* **41**, 219–239 (1993).
40. Inoue, A. et al. Application of chemical geothermometry to low-temperature trioctahedral chlorites. *Clays Clay Min.* **57**, 371–382 (2009).
41. Powolny, T., Słowik, M. D., Anczkiewicz, A. A. & Jaworowska, M. S. Origin and timing of spilitic alterations in volcanic rocks from Głuszyca Górna in the Intra Sudetic Basin, Poland. *Sci. Rep.* **12**, 1–26 (2022).
42. Shau, Y. H., Peacor, D. R. & Essene, E. J. Corrensite and mixed-layer chlorite/corrensite in metabasalt from northern Taiwan: TEM/AEM, EMPA, XRD, and optical studies. *Contrib. Miner. Petrol.* **105**, 123–142 (1990).
43. Kolesov, B. A. & Geiger, C. A. Raman spectra of silicate garnets. *Phys. Chem. Min.* **25**, 142–151 (1998).
44. Fu, M., Dai, J. & Zhao, L. A study on the Raman spectral characteristics of garnet from the Jiama copper polymetallic deposit in Tibet. *Minerals* 12, (2022).
45. Gunasekaran, S., Anbalagan, G. & Pandi, S. Raman and infrared spectra of carbonates of calcite structure. *J. Raman Spectrosc.* **37**, 892–899 (2006).
46. De Andrade, J. E., Machado, R., Macêdo, M. A. & Cunha, F. G. C. AFM and XRD characterization of silver nanoparticles films deposited on the surface of DGEBA epoxy resin by ion sputtering. *Polimeros* **23**, 19–23 (2013).
47. Henmi, C., Kusachi, I., Henmi, K. & Morimotoite $Ca_3TiFe^{2+}Si_3O_{12}$, a new titanian garnet from Fuka, Okayama Prefecture, Japan. *Mineral. Mag.* **59**, 115–120 (1995).
48. Basso, R., Della Giusta, A. & Zefiro, L. Crystal structure refine-ment of plazolite: a highly hydrated natural hydrogrossular. *Neues Jahrbuch fur Mineralogie Abhandlungen* 251–258 (1983).
49. Armbruster, T. Structure refinement of hydrous andradite, $Ca_3Fe_{1.54}Mn_{0.20}Al_{0.26}(SiO_4)_{1.65}(O_4H_4)_{1.35}$, from the Wessels mine, Kalahari manganese field, South Africa. *Eur. J. Mineral.* **7**, 1221–1226 (1995).
50. Huang, H. M. et al. Revealing the secrets behind the color and sea-wave patterns of Larimar. *Minerals* **13**, 1221 (2023).
51. Chen, H. F. et al. Dissolution of Na2O · CaO · nSiO2 glasses in Na2CO3 solution for long-term and short-term experiments. *J. Non Cryst. Solids*. **351**, 1417–1425 (2005).
52. Hara, J. & Tsuchiya, N. Chemical modification of pyroclastic rock by hot water: an experimental investigation of mass transport at the fluid-solid interface. *Geofluids* **9**, 24–38 (2009).
53. Beard, J. S. & Hopkinson, L. A fossil, serpentinization-related hydrothermal vent, Ocean Drilling Program Leg 173, Site 1068 (Iberia Abyssal Plain): some aspects of mineral and fluid chemistry. *J. Geophys. Res. Solid Earth*. **105**, 16527–16539 (2000).
54. Buse, B., Schumacher, J. C., Sparks, R. S. J. & Field, M. Growth of bultfonteinite and hydrogarnet in metasomatized basalt xenoliths in the B/K9 kimberlite, Damtshaa, Botswana: insights into hydrothermal metamorphism in kimberlite pipes. *Contrib. Miner. Petrol.* **160**, 533–550 (2010).
55. Cheng, W., Greenwood, H. J., Hu, H. & Frost, D. C. XRD and XPS analyses of the grossular-hydrogrossular series. *Can. Mineral.* **28**, 87–91 (1990).
56. Yavuz, F., Kumral, M., Karakaya, N., Karakaya, M. T. & Yildirim, D. K. A Windows program for chlorite calculation and classification. *Comput. Geosci.* **81**, 101–113 (2015).

Acknowledgements

Jerzy Czerny is gratefully acknowledged for his constructive comments during the initial investigations of hydrous garnets. Maciej Sitarz is thanked for his support at the stage of measurements carried out using Raman microscopy. We are very grateful to Raúl Lira and the anonymous reviewer for their comments and suggestions, which enabled us to substantially improve the first version of the manuscript. The handling of our manuscript by Fei Qi and Ganesh Giram is also highly appreciated.

Author contributions

J.W. conceived and designed the analyses; M.D-S., W.H., L.N-N. wrote the main manuscript; A.W. made and interpreted EMP analyses and wrote the main text of the manuscript; A.G. made and interpreted XRD analyses and calculated the unit cell parameter of garnet; P.J. made micro-Raman measurements; M.P. and R.M. did geological field works. All authors reviewed and edited the final version of the manuscript.

Declarations

Competing interests

The authors declare no competing interests.

Additional information

Supplementary Information The online version contains supplementary material available at https://doi.org/10.1038/s41598-024-81479-8.

Correspondence and requests for materials should be addressed to M.D.-S.

Reprints and permissions information is available at www.nature.com/reprints.

Publisher's note Springer Nature remains neutral with regard to jurisdictional claims in published maps and institutional affiliations.